RICE UNIVERSITY

Applying the Short-Time Direct Directed Transfer Function to Human Electrocorticographic Recordings from a Language Task

by

Meagan Lee Whaley

A Thesis Submitted
in Partial Fulfillment of the
Requirements for the Degree

Master of Arts

Approved, Thesis Committee:

Steven Cox
Professor, Computational and Applied Mathematics

Mark Embree
Professor, Computational and Applied Mathematics

Yuri Dabaghian
Assistant Professor, Computational and Applied Mathematics

Nitin Tandon
Associate Professor, The Vivian L. Smith Department of Neurosurgery

Houston, Texas
May, 2012

RICE UNIVERSITY

Applying the Short-Time Direct Directed Transfer Function to Human Electrocorticographic Recordings from a Language Task

by

Meagan Lee Whaley

A Thesis Submitted
in Partial Fulfillment of the
Requirements for the Degree

Master of Arts

Approved, Thesis Committee:

Steven Cox
Professor, Computational and Applied Mathematics

Mark Embree
Professor, Computational and Applied Mathematics

Yuri Dabaghian
Assistant Professor, Computational and Applied Mathematics

Nitin Tandon
Associate Professor, The Vivian L. Smith Department of Neurosurgery

Houston, Texas
May, 2012

ABSTRACT

Applying the Short-Time Direct Directed Transfer Function to Human Electrocorticographic Recordings from a Language Task

by

Meagan Lee Whaley

This thesis applied the short-time direct directed transfer function (SdDTF) to time series data recordings from intracranial electrodes that measure the brain's electrical activity to determine the causal influences that occurred between brain regions during a speech production task. The combination of high temporal and spatial resolution of the electrocorticography (ECoG) recordings directly from the cortex render these measurements of brain activity desirable, particularly when analyzing the fine cognitive dynamics involved in word generation. This research applied a new method to characterize the SdDTF results by compressing across time and high gamma frequencies, generating adjacency matrices, and graphing them to visualize the influences between anatomical regions over the duration of the entire task. This consolidated SdDTF analysis technique allowed for data from a total of seven patients to be combined, generating results which were consistent with current speech production models. The results from this thesis contribute to the expansion of language research by identifying areas relevant to word generation, providing information that will help surgeons avoid irreparable damage to crucial cortex during brain surgery.

Acknowledgments

The unconditional, unwavering support and love from my family and dear friends led me to where I am today. Thank you to my mother and father, for guiding me, allowing me to make my own decisions, and supporting my happiness above all else. Thank you to Cass, my other half, for patiently listening, sharing, and understanding in the good times and the bad. Thank you to Jim, for always being my protector and providing a sturdy foundation in my life. Thank you to Kora, for reminding me how to count to ten, particularly on the tough days, and thank you to Matt, Nicole, Ricardo, Jorge, Cynthia, and Yin for their kindness and love.

Working for Dr. Cox has been an adventure. His patience and kind instruction have taught me many lessons this past year, and I look forward to learning many more. I would like to thank my committee members for their support, as well as Dr. Tandon and Chris Conner, for presenting their research in CAAM 499 last year. The mentorship and collaboration between Dr. Tandon, Chris, Dr. Cox, and myself has exposed me to a side a neuroscience for which I feel very fortunate to be a part of.

Thank you to all of the data collection and processing done by Chris and Tom in Tandon Research Lab, as well as the friendly support from Kiefer, Cihan, and the students of CAAM 499. Lastly, thank you to the National Science Foundation for the financial support that has allowed me to study and research at Rice University (NSF: DMS-0739420, EMSW21-VIGRE: Leveraging the Strength and Extending the Reach of an Integrated Mathematics Community).

Contents

Illustrations

Tables

Chapter 1

Introduction

1.1 Connecting Language to Time Series

This research used recordings from intracranial electrodes to determine the causal influences between brain regions that occurred during a word generation task. The intracranial electrodes were implanted in patients who suffered from recurring seizures not successfully managed by medication, a condition referred to as intractable epilepsy. If the source of recurrent seizures can be localized to a specific region of the brain, one treatment option is the removal of the problematic brain tissue through resective surgery. Prior to resection, the seizure onset location is more precisely determined by implanting grids of electrodes on the outer surface of the brain and monitoring "cerebral activity" over a period of days (Ritaccio et al. [16]). The technique of recording from intracranial electrodes is referred to as electrocorticography, or ECoG. Although invasive, this ECoG is implemented because it provides the "best spatial and temporal resolution of epileptiform activity" [16].

While being monitored for seizure localization, the seven patients who participated in this study consented to complete a series of language and memory tasks. This research analyzed the intracranial electrode recordings from a verb generation

task called Wordstem to investigate the mechanisms involved in processing a visual stimulus to produce a verbal response. When it comes to understanding the underlying mechanisms involved in language production, humans are the ideal candidates to study, which is why "language is understood far less than sensation, memory, or motor control, because language has no animal homologs, and methods appropriate to humans [functional magnetic resonance imaging (fMRI), studies of brain-damaged patients, and scalp-recorded potentials] are far coarser in space or time than the underlying causal events in neural circuitry" (Sahin [18]). Therefore, the patients being monitored for seizure localization offer a unique opportunity in the field of language research, as the ECoG recordings are more resolute in time and space.

This work investigated the neural activations that occurred during the process of responding to a collection of visual stimuli through speech. According to Sahin et al., Levelt, Roelofs, and Meyer constructed "the most comprehensive model of speech production," which contains multiple sequential stages, each with a specific and unique purpose and a duration on the order of milliseconds (Sahin et al. [18]; Levelt et al. [12]). Hence, temporal precision is an important factor to consider when addressing questions of the dynamics involved in language production. Additionally, high spatial resolution is ideal when identifying the roles of regions during tasks, as areas of the brain that are near to each other (within 1 cm) may have vastly different functionalities (Edward et al. [7]).

While this research studied ECoG recordings generated by "electrical activity of

the brain," it is important to explore other recording methods (Nunez and Katznelson, Ch. 1 [15]). Electroencaphalography (EEG), fMRI, and magnetoencephalography (MEG) are three recording techniques that share the attractive quality of being non-invasive, painfree procedures. They differ in the sources of activation being measured, as well as the precision of the measurements. EEG is a method of recording electricity generated by synchronous activity of large groups of neurons through electrodes placed on the scalp, which allows for high spatial coverage (Nunez and Katznelson [15]). The tissue and bone separating the brain from the electrodes averages the neuronal activity, thus EEG loses any asynchronous behavior or activity from smaller populations of neurons. While scalp electrodes can potentially record from a wide range of regions, the physiological interference and averaging render this technique suboptimal (Ritaccio et al. [16]).

fMRI is an imaging technique with high spatial coverage and resolution, and its measurements are generated by the blood flow that occurs in response to an "event" (in the context of this research, the event is each visual stimulus). However, fMRI is limited in its temporal resolution because hemodynamic responses (resulting from blood movement) are more delayed than electrical responses in the brain, resulting in a time lag in the fMRI measurements. Hence, it may be less preferable than more temporally precise methods (Brookes et al. [1]). MEG is another imaging technique, but it measures "magnetic fields which are produced by electrical activity of the brain" (Cohen [2]). Alternative to fMRI, MEG has high temporal resolution

but it suffers from less spatially resolute measurements (Levelt et al. [13]; Edwards et al. [7]). As previously mentioned, highly precise recording techniques are ideal when studying language, so although scalp EEG, fMRI, and MEG are noninvasive methods capable of wide spatial coverage, they lack the combination of high spatial and temporal resolution desired for this research.

Electrocorticography, the more invasive analogue of EEG, offers a rare opportunity to overcome issues of "coarse" measurements encountered with fMRI, scalp EEG, or MEG (Sahin [18]; Ritaccio et al. [16]). It is defined as the process of "recording the EEG directly from the surface of the brain" (Ritaccio et al., [16]). As the electrodes are surgically implanted on the brain, skull and tissue are bypassed, reducing physiological interference in the recordings. Additionally, the sampling rate used for the recordings analyzed in this research was 1000 Hz (one data point per millisecond), yielding measurements capable of capturing more enhanced temporal dynamics than fMRI. Finally, ECoG recordings are capable of capturing more dynamical and localized behavior, such as asynchronous neuronal activity lost by scalp EEG or "electrophysiological signals" caused by smaller groups of neurons (Ritaccio et al. [16]).

It is important to note that ECoG recordings do indeed suffer in some aspects. First, 60 Hz "noise" due to electrical recording equipment and/or epileptiform activity (seizure-like brain activity occurring between seizures) are undesirable entities that can (and frequently do) taint the recordings (see Section 2.1 for how data is handled to

address these issues). In addition, these recordings are incapable of capturing activity at the single-neuron level, which may be a drawback in some lines of research. Lastly, electrode locations are selected for medical purposes (paying no mind to language research), so lack of spatial coverage is a pervasive issue in ECoG research (Edwards et al. [7]; Crone et al. [11] and [10]). However, due to the number of patients involved in this study, the combined spatial coverage of their electrodes makes this less of a concern. Despite these disadvantages (including the obvious invasiveness of the implantation procedure), recordings from intracranial electrodes are viewed as offering the high spatial and temporal precision desired when studying speech production.

The precise ECoG recordings studied in this research measured neuronal activity under electrodes generated during the Wordstem task. In general, "synchronized rhythmic discharges" of neurons are seen in the ECoG recordings via oscillatory behavior and "are of interest because they indicate organized activity" (Singer [20]). Research in oscillatory behavior of neuronal populations has led to the identification of frequency ranges that are characteristic of specific behaviors. For instance, activity in the delta range ($0.5 - 4\,\text{Hz}$) occurs during sleep, and activity in occipital areas around $10\,\text{Hz}$ (within the alpha range) is observed during stages of drowsiness or relaxedness. Higher frequency ranges ($> 15\,\text{Hz}$) are "particularly pronounced in awake performing brains" and have been linked to tasks requiring sensory and motor processing (Singer [20]).

More complicated tasks (such as word production) require the recruitment of larger networks of neurons, and neural activity at higher oscillations is believed to be significant during such tasks. The gamma frequency range (defined in this research to be $30-240\,\text{Hz}$) is widely studied in ECoG language research, as oscillations in this range are believed to indicate the presence of large-scale cortical processing and to be involved in "task-dependent activations" (Edwards et al. [7]). Indeed, ECoG studies investigating this frequency range have drawn valid conclusions about activations occurring during language tasks (Singer [20]; Crone et al. [10], [11]; Edwards et al. [7]). Motivated by these studies, the $60-150\,\text{Hz}$ subset of the high gamma frequency range was selected for this study.

While the ECoG studies researched for this thesis converge on analyzing high gamma frequencies, they differ in the analysis techniques. Some studies addressed questions of "when" and "where" activations occur, while other studies addressed deeper issues, such as causal influences occurring between regions during the administered task. This research took the latter approach, and Granger causality is a foundational tool for this type of analysis.

Granger causality begins with the concept that a time series signal (such as an ECoG recording from one electrode) at time t can be modeled as a linear combination of the same signal at a discrete set of prior time points, plus some additional error. If the incorporation of a second series (such as an ECoG recording from another electrode) into the model improves the variance of the original error, the second

series is said to have a "causal influence on the first" (section 17.5, Schelter [6]). This concept can be extended to multi-dimensional models, where causal flow can be transferred through intermediate signals (section 17.5, Schelter [6]). This idea has powerful implications when applied to electrophysiological recordings, for if the model were generated from recordings from specific regions of the brain during a language task, the resulting causal influences would be indicative of the mechanisms and interrelations involved in speech production.

Studying high gamma frequencies was previously stressed, so determining a method to extend the causal analysis from the time domain to the spectral domain was of great importance. Beginning in the time domain, the Multivariate Autoregressive model (MVAR) was the technique used because it allows for simple transformations to frequency representations. The short-time direct directed transfer function (SdDTF) was used as the primary method of analysis in the frequency domain firstly because it is easily derived from the MVAR model. More importantly, the SdDTF was selected because it is a method of measuring the "directions, intensities, and spectral contents of direct causal interactions between signals" [10]. The results from the SdDTF applied to ECoG data, therefore, provide information about the direct causal influences occurring between regions underneath electrodes at specific frequencies, which aligns with the goal of identifying cortical locations most relevant to speech production during a language task.

Upon solving for the SdDTF values from the ECoG time series data, a simplifi-

cation across time and frequency was made to enable consolidation across all seven patients and to perform graphical analysis to visualize the causal influences. Following implementation, this technique was verified with results that are in line with current models of speech production. Before proceeding, however, a brief statistical framework will be presented in the following section, as these concepts are fundamental to the derivation of the time series model.

1.2 Statistical Framework for Time Series

For a total of N equally-spaced time points, the electrophysiological recordings from M electrodes are defined as the time series $\mathrm{X} \in \mathbb{R}^{M \times N}$. The time domain is the same for each electrode from each patient, and it was selected such that the experimental trials (including pre-stimulus to articulation time) were covered. In order to quantify the interactions between the data from all electrodes, an analytic representation, or model, is desired, preferably one that will facilitate analysis in the frequency domain. The phenomenological linear model is a simple and natural place to begin, and following the lead of other works that analyzed ECoG data, the Multivariate Autoregressive model (MVAR) was selected (Crone et al., [10] and [11], Ding et al., [5]).

The derivation of the MVAR model begins with assumptions about the statistical properties of each time series. Hence, definitions and motivation will be provided before proceeding (the notational conventions and order of definitions follow section 4.3 of Marple [17]).

Let $X^i(t)$ denote the i^{th} trial at time t of a random process X $\in \mathbb{R}^{1\times N}$(such as a recording from a single electrode over multiple trials of a language task). For N total trials, the **mean** or **expected value** at time t is defined as

$$E\left[X(t)\right] = \frac{1}{N}\sum_{j=1}^{N} X^j(t) \equiv \overline{X}(t).$$

The **autocorrelation** of a random process X at times t and s is given by

$$r_{XX}(t,s) = E\left[X(t)X^*(s)\right].$$

For two random processes X and Y, the **cross correlation function** is

$$r_{XY}(t,s) = E\left[X(t)Y^*(s)\right].$$

Some texts include a normalization factor in the correlation functions, but following Marple's text, this factor is excluded. The autocovariance at times t and s is

$$\begin{aligned} c_{XX}(t,s) &= E\left[\left(X(t) - \overline{X}(t)\right)\left(X^*(s) - \overline{X}^*(s)\right)\right] \\ &= E\left[X(t)X^*(s)\right] - \overline{X}(t)\overline{X}^*(s) \\ &= r_{XX}(t,s) - \overline{X}(t)\overline{X}^*(s). \end{aligned}$$

The **cross covariance** is the analogous covariance function for two random processes, X and Y, and it is defined as

$$\begin{aligned} c_{XY}(t,s) &= E\left[\left(X(t) - \overline{X}(t)\right)\left(Y^*(s) - \overline{Y}^*(s)\right)\right] \\ &= E\left[X(t)Y^*(s)\right] - \overline{X}(t)\overline{Y}^*(s) \\ &= r_{XY}(t,s) - \overline{X}(t)\overline{Y}^*(s). \end{aligned}$$

Two random processes are uncorrelated if $c_{XY}(t,s) = 0$ for all t and s (section 4.3, Marple [17]). **Stationary** processes are a special class of processes whose statistical properties do not vary with time. **Wide-sense stationary** processes are a subset of stationary processes characterized by time-independent mean and correlation functions:

$$\overline{X}(t) = \overline{X}$$

$$r_{XX}(t, t+\tau) = r_{XX}(\tau) \qquad \forall t.$$

Similarly, the cross correlation function of **jointly** wide-sense stationary processes is time independent:

$$r_{XY}(t, t+\tau) = r_{XY}(\tau) \qquad \forall t.$$

Important properties of the correlation functions of wide-sense stationary processes include

$$r_{XX}(-t) = r^*_{XX}(t) \tag{1.1}$$

$$r_{XY}(-t) = r^*_{YX}(t). \tag{1.2}$$

Ergodic processes are a class of random processes whose ensemble averages can be replaced by time averages; hence, meaningful statistics may be drawn from a single trial. Furthermore, such processes may be **autocorrelation ergodic**, a property that will prove useful when working with empirical data (section 4.4, Marple [17]). For a time lag of m, a consequence of an autocorrelation ergodic random process is

$$\lim_{M\to\infty} \frac{1}{2M+1} \sum_{n=-M}^{M} X(n+m)X^*(n) = r_{XX}(m). \tag{1.3}$$

Given a wide-sense stationary, zero mean, autocorrelation ergodic time series X at time t and lag k with dimension n (where n is the total number of channels, and X_i denotes the i^{th} component of X), we define the multidimensional expectation (over time) between $X(t)$ and $X^*(t-k)$ as

$$
\begin{aligned}
E\left[X(\cdot)X^*(\cdot-k)\right] &= \begin{bmatrix} E\left[X_1(\cdot)X_1^*(\cdot-k)\right] & \dots & E\left[X_1(\cdot)X_n^*(\cdot-k)\right] \\ E\left[X_2(\cdot)X_1^*(\cdot-k)\right] & \dots & E\left[X_2(\cdot)X_n^*(\cdot-k)\right] \\ \dots & \dots & \dots \\ E\left[X_n(\cdot)X_1^*(\cdot-k)\right] & \dots & E\left[X_n(\cdot)X_n^*(\cdot-k)\right] \end{bmatrix} \\
&= \begin{bmatrix} c_{X_1X_1}(t,t-k) & \dots & c_{X_1X_n}(t,t-k) \\ c_{X_2X_1}(t,t-k) & \dots & c_{X_2X_n}(t,t-k) \\ \dots & \dots & \dots \\ c_{X_n,X_1}(t,t-k) & \dots & c_{X_nX_n}(t,t-k) \end{bmatrix} \\
&= \begin{bmatrix} r_{X_1X_1}(t,t-k) & \dots & r_{X_1X_n}(t,t-k) \\ r_{X_2X_1}(t,t-k) & \dots & r_{X_2X_n}(t,t-k) \\ \dots & \dots & \dots \\ r_{X_n,X_1}(t,t-k) & \dots & r_{X_nX_n}(t,t-k) \end{bmatrix} \\
&\equiv R_{XX}(-k),
\end{aligned}
$$

where $R_{XX}(-k)$ is the covariance matrix of X at lag k. Note that the covariance matrix is equivalent to the correlation matrix in this instance because the process is assumed to have zero mean. In summation, for a wide-sense stationary, zero mean,

autocorrelation ergodic time series X,

$$E\left[X(t)X^*(t-k)\right] = R_{XX}(-k) = R^*_{XX}(k) \tag{1.4}$$

where stationarity (specifically (1.2)) allowed for the symmetric property.

The early definitions of this section can thus be easily be extended to multidimensional random processes. The definitions and notational conventions presented will be used when deriving the time series model in the following chapter, which also explores topics of data collection, preprocessing, implementation, and analysis techniques.

Chapter 2

Methods

2.1 Experimental Data Acquisition and Methods

This thesis defined the recordings from intracranial electrodes as time series to determine the causal influences occurring between brain regions during a specific language task. The time series recordings were obtained from grids of electrodes implanted in seven patients for seizure localization (see Figure 2.1). Hence, using the notation from Chapter 1, $X(t)$ is a multi-dimensional matrix of time series data, whose i^{th} row represents the ECoG recording of the i^{th} electrode at time t. For more detailed information concerning equipment, surgical implantation, and imaging techniques for electrode localization, see Conner et al. [3].

The ECoG data for this study was obtained from recordings taken during the Wordstem language task, which required the subjects to verbally form complete words from incomplete words presented on a computer monitor. Every patient was shown a diverse collection of visual stimuli (approximately 80 total trials, with one trial being a single stimulus), and the subjects were to verbally respond to each stimulus with the first word that came to mind that transformed the word fragment into a complete *action* word. For example, the stimulus "RU_" could be completed with "RUN" or

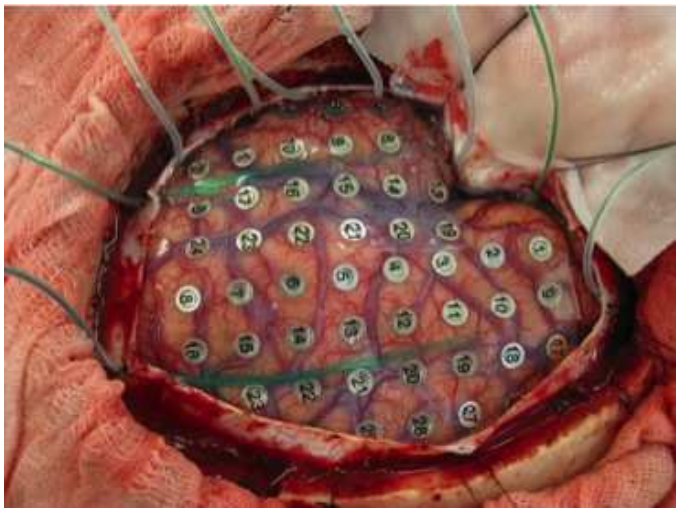

Figure 2.1 : Picture taken during surgical implantation of electrodes (Tandon, [21]).

"RUIN" for a correct response, but "RUM" would be counted as incorrect, as it is not an action word. No restriction was placed on the length of the response word.

Following the data exportation into Matlab, each trial and electrode was manually reviewed using in-house software to exclude those with excessive epileptiform activity, 60 Hz noise, and areas to be resected from the analysis. Additionally, incorrect trials (those answered with non-action words or those with no response) were excluded. Table 2.1 below summarizes the final electrode and trial counts for each patient used in this study. While reviewing literature for this research, some studies included a subset of implanted electrodes, but Mullen states that it is ideal to use "*all* available variables" [14]. As such, data from all available electrodes was used in constructing each model.

Each trial was shifted in time such that the initial presentation of stimulus corresponded to 0 ms, and the overall epoch analyzed for each trial was from -500 ms

Patient ID	Number of Electrodes	Number of Trials
ta355	86	49
ta356	79	56
ta401	87	44
ta408	62	53
ta439	91	59
ta442	94	46
ta451	72	51

Table 2.1 : Final electrode and trial counts for each subject following the exclusion of incorrect trials and channels with excessive 60 Hz noise or epileptiform activity.

to 2500 ms. Figure 2.2 depicts a trial averaged ECoG recording during the −500 to 2500 ms epoch recorded from an electrode implanted in the pars triangularis gyrus of a patient during the Wordstem task.

This Figure illustrates the time series data prior to applying computational analysis. The goal of this research is to gain meaning from such series, in particular determining causal influences present in the underlying brain regions that occur during language production. The first step in such an analysis is to build a model of the time series data, and the method selected for this research is presented in the next section.

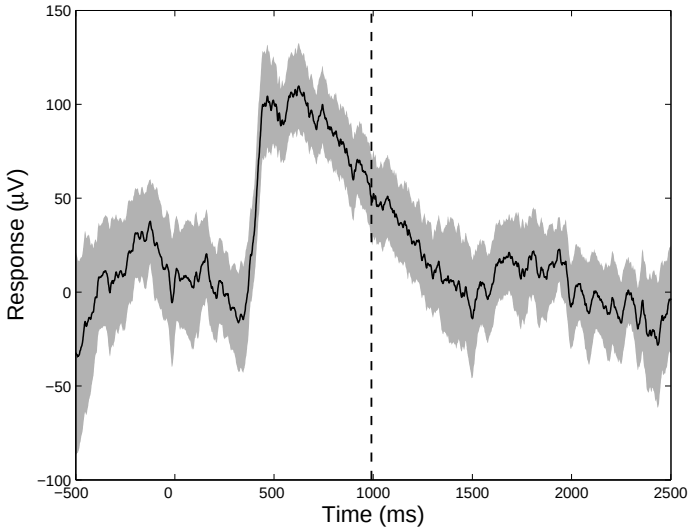

Figure 2.2 : The trial average of a single electrode ±2 standard errors of the mean of time series signals recorded during the Wordstem task, with trial average articulation onset (or reaction time) indicated by the vertical dashed line.

2.2 Derivation of Time Series Model

The Multivariate Autoregressive model stands as the basis for modeling the experimental data, and it relies on the statistical background presented in the Section 1.2. Assuming initial assumptions are met, the MVAR model expresses the data at the current time as a linear combination of prior data, plus additional error. This simple representation allows for straightforward analysis in the frequency domain, and as high gamma frequencies are of particular interest in this research, MVAR is an attractive and natural method to use.

Given a wide-sense stationary, zero mean, autocorrelation ergodic time series X at

time t with dimension n, the goal of the model is to determine coefficients $A(j) \in \mathbb{R}^{n\times n}$ and model order p such that

$$X(t) + \sum_{j=1}^{p} A(j)X(t-j) = \varepsilon(t), \tag{2.1}$$

where $\varepsilon(t)$ is a zero mean error term uncorrelated with any of the prior time series data, that is, for $j > 0$,

$$\begin{aligned} E\left[(\varepsilon(t) - \overline{\varepsilon})\left(X(t-j) - \overline{X}\right)^*\right] &= R_{\varepsilon X}(t, t-j) - \overline{\varepsilon}\overline{X}^* \\ &= R_{\varepsilon X}(-j) \\ &= 0. \end{aligned}$$

Note that for this research, dimension n varies by patient and corresponds to the number of electrodes implanted (see Table 2.1), where at fixed time t, $X(t)$ is an n-dimensional vector, with the i^{th} entry corresponding to the electrophysiological data recorded from electrode i at time t.

The first unknowns solved for in (2.1) are the coefficient matrices, and their derivation will follow Ding's 2006 work (section 17.5, [6]). For a given model order p and $k = 1, 2, \ldots p$, first right multiply (2.1) by $X^*(t-k)$

$$X(t)X^*(t-k) + \sum_{j=1}^{p} A(j)X(t-j)X^*(t-k) = \varepsilon(t)X^*(t-k).$$

Next, expectations are taken over trials, but by ergodicity, this is equivalent to expectations over time:

$$E\left[X(t)X^*(t-k) + \sum_{j=1}^{p} A(j)X(t-j)X^*(t-j)\right] = E\left[\varepsilon(t)X^*(t-k)\right].$$

By linearity of $E[\cdot]$, the equation becomes:

$$E\left[X(t)X^*(t-k)\right] + \sum_{j=1}^{p} A(j)E\left[X(t-j)X^*(t-k)\right] = E\left[\varepsilon(t)X^*(t-k)\right].$$

Because $\varepsilon(t)$ is uncorrelated with the prior time series data, the right-hand side is zero, so by definition (1.4), the system is reformulated as:

$$R_{XX}(-k) + \sum_{j=1}^{p} A(j)R_{XX}(j-k) = 0, \quad k = 1, \ldots, p, \tag{2.2}$$

which are known as the Yule-Walker equations. Equation (2.2) consists of precisely p matrix equations for the p unknown coefficient matrices.

The model order (p in Equation (2.1)) is the remaining unknown variable needed to solve for the MVAR model, and it depends on the auto covariance of $\varepsilon(t)$:

$$\Sigma \equiv E\left[\varepsilon(t)\varepsilon^*(t)\right].$$

The "best" (standard practice) order corresponds to the value which minimizes the Akaike Information Criterion (AIC) or Bayesian Information Criterion (BIC). Hence, Equation (2.1) is solved over a range of orders, the AIC and BIC values are determined for each order, and the order that minimizes the AIC or BIC is used when solving the final MVAR model.

For dimension n and order m, these criteria are defined as

$$AIC(m) = 2\ln(\det\Sigma(m)) + \frac{2n^2m}{N_{total}} \tag{2.3}$$

$$BIC(m) = 2\ln(\det\Sigma(m)) + \frac{2n^2m\log(N_{total})}{N_{total}}, \tag{2.4}$$

where N_{total} is the total number of data points across all trials (section 17, Ding et al. [6]). Both values do not necessarily obtain minima at the same order, and Ding et al. claim that BIC may be better suited for ECoG studies, as N_{total} is typically larger in this field (section 17, Ding et al. [6]). The $\Sigma(m)$ notation is used to emphasize the dependence of Σ on the model order, as the covariance matrix is not constant across all orders. Refer to Table 2.3 for the AIC and BIC values used for the empirical data.

Now that all of the necessary pieces to represent the time series data as in Equation (2.1) have been presented, we must quantify causal influence before extending the analysis into the frequency domain, and Granger Causality is the concrete tool for this quantification.

2.3 Quantifying Causal Influence

Granger Causality is a quantification of the concept of causal influence, which was introduced in Section 1.1. It can be applied to multi-channel time series data to determine direct influences within the system, and the two-channel system is a simple, illustrative starting point.

Let $X, Y \in \mathbb{R}^{1\times N}$ be two time series such that their MVAR models are:

$$\sum_{j=0}^{p_1} A(j)X(t-j) = \varepsilon_1(t) \qquad var(\varepsilon_1(t)) = \Sigma_1 \tag{2.5}$$

$$\sum_{j=0}^{p_2} B(j)Y(t-j) = \eta_1(t) \qquad var(\eta_1(t)) = \Gamma_1 \tag{2.6}$$

where *var* denotes variance and is indicative of the error of the model. Upon increasing

the dimension of models, the new, 2-dimensional MVAR model is formulated:

$$\sum_{j=0}^{p_3} \begin{bmatrix} \tilde{A}(j) & \tilde{C}(j) \\ \tilde{B}(j) & \tilde{D}(j) \end{bmatrix} \begin{bmatrix} X(t-j) \\ Y(t-j) \end{bmatrix} = \begin{bmatrix} \varepsilon_2(t) \\ \eta_2(t) \end{bmatrix} \quad \begin{matrix} var(\varepsilon_2(t)) = \Sigma_2 \\ var(\eta_2(t)) = \Gamma_2 \end{matrix} . \tag{2.7}$$

Letting Υ_2 be the covariance between X and Y, the full covariance matrix for the 2-dimensional MVAR model is

$$\Sigma = \begin{bmatrix} \Sigma_2 & \Upsilon_2 \\ \Upsilon_2 & \Gamma_2 \end{bmatrix} \tag{2.8}$$

Recall that if the addition of a second series significantly reduces the error of the original model, then the second series is said to have a causal influence on the first. In the case of this bivariate MVAR model, the causal influence that series Y has on series X is defined as:

$$F_{Y \to X} = \ln \frac{\Sigma_1}{\Sigma_2} \tag{2.9}$$

Hence, if the variance of X (defined as the error of the original 1-dimension model, Σ_1) has not improved with the inclusion of Y and $\Sigma_2 = \Sigma_1$, then $F_{Y \to X} = 0$, which signifies a lack of causal influence from Y to X. Alternatively, if the error has improved and $\Sigma_2 < \Sigma_1$, then $\frac{\Sigma_1}{\Sigma_2} > 1$, and $F_{Y \to X}$ will be nonzero. Similarly, the causal influence that series X has on series Y is defined as:

$$F_{X \to Y} = \ln \frac{\Gamma_1}{\Gamma_2} \tag{2.10}$$

which can be interpreted in the same manner as $F_{Y \to X}$ (section 17.5, Ding et al. [6]).

Continuing with the bivariate case, causality is next formulated in the frequency domain, where the discrete Fourier transform of Equation (2.1) is taken to derive the

transfer function. Rewriting Equation (2.1) with $A(0) = Id(n)$, where $Id(n)$, is the $n \times n$ dimensional identity matrix:

$$\sum_{j=0}^{p} A(j)X(t-j) = \varepsilon(t).$$

Inserting convolution notation, this equation is equivalent to:

$$A(t) \star X(t) = \varepsilon(t).$$

Take the Fourier transform of both sides of the equation, use the convolution property, and solve for $\widehat{X}(\omega)$:

$$\widehat{X}(\omega) = \widehat{A}(\omega)^{-1}\widehat{\varepsilon}(\omega),$$

where $\widehat{A}^{-1}$ is defined to be the **transfer function** H (Crone et al., [10], Kamiński et al. [9]):

$$H(\omega) \equiv \widehat{A}(\omega)^{-1} = \left(\sum_{j=0}^{p} A(j)e^{-i2\pi j\omega\Delta t}\right)^{-1} \tag{2.11}$$

A nonzero element in the $(i,j)^{th}$ entry of the transfer function indicates the transfer of Granger causality from channel j to channel i at a particular frequency (Kamiński et al., [9]). As transfer is not necessarily equal in opposite directions, note that H is asymmetric. One additional aspect of the transfer function is that it does not compensate for indirect, intermediate transference, as is the case pictured in Figure 2.3 where Node 2 behaves as the intermediate vehicle of signal transference from Node 1 to Node 3 (Crone et al., [10]).

The spectral matrix, S_{XX}, is necessary for the formulation of Granger causality in the spectral domain, and it is defined as the Fourier transform of the autocorrelation

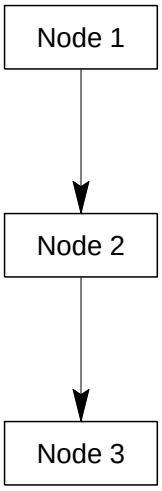

Figure 2.3 : Example of intermediate, indirect causal transfer from Node 1 to Node 3 via Node 2. The transfer function would not distinguish this scenario from a direct transfer from Node 1 to Node 3. A numerical example is implemented to further illustrate this scenario.

of X. Its formula is given by

$$S_{XX}(\omega) \equiv \widehat{R_{XX}}(\omega) = H(\omega)\Sigma H^*(\omega), \tag{2.12}$$

with the following partition in the bivariate example

$$S_{XX}(\omega) = \begin{bmatrix} s_{XX}(\omega) & s_{XY}(\omega) \\ s_{YX}(\omega) & s_{YY}(\omega) \end{bmatrix}.$$

In order to distinguish between changes due to internal sources (or "intrinsic" power increases) or the other series of the model ("causal" power increases), a transformation is performed on the Fourier transform of the MVAR model (section 17.5,

Ding et al., [6]). The first transformation matrix is

$$P_1 = \begin{bmatrix} 1 & 0 \\ -\frac{\Upsilon_2}{\Sigma_2} & 1 \end{bmatrix}. \tag{2.13}$$

Beginning with the Fourier transform of Equation (2.1):

$$\widehat{A}(\omega)\widehat{X}(\omega) = \widehat{\varepsilon}(\omega).$$

Left multiply by P_1, and take the inverse to solve for $\widehat{X}(\omega)$:

$$\widehat{X}(\omega) = \left(P_1\widehat{A}(\omega)\right)^{-1} P_1\widehat{\varepsilon}(\omega),$$

which yields a new transfer function, $\overline{H}(\omega) \equiv \left(P_1\widehat{A}(\omega)\right)^{-1}$. Similar to the spectral matrix, let $\overline{H}$ have the following decomposition:

$$\overline{H}(\omega) = \begin{bmatrix} \overline{h}_{XX}(\omega) & \overline{h}_{XY}(\omega) \\ \overline{h}_{YX}(\omega) & \overline{h}_{YY}(\omega) \end{bmatrix}.$$

From these definitions, the causal influence from Y to X is defined as

$$f_{Y\to X}(\omega) = \ln \frac{s_{XX}(\omega)}{\overline{h}_{XX}(\omega)\Sigma_2\overline{h}^*_{XX}(\omega)}, \tag{2.14}$$

where the numerator is interpreted as the intrinsic power of X plus the causal power of X attributable to Y, and the denominator is simply the intrinsic power of series X at frequency ω. Hence, if the causal power Y on X is negligible, this will render a zero $f_{Y\to X}$. A nonzero causal power will correspondingly yield nonzero causal influence $f_{Y\to X}$.

In order to determine the causal influence of Y due to X, a second transformation matrix P_2 is introduced:

$$P_2 = \begin{bmatrix} 1 & -\frac{\Upsilon_2}{\Gamma_2} \\ 0 & 1 \end{bmatrix}. \tag{2.15}$$

Following the same steps, a second transfer function, $\tilde{H}(\omega) \equiv \left(P_2\widehat{A}(\omega)\right)^{-1}$ is found for the bivariate case:

$$\tilde{H}(\omega) = \begin{bmatrix} \tilde{h}_{XX}(\omega) & \tilde{h}_{XY}(\omega) \\ \tilde{h}_{YX}(\omega) & \tilde{h}_{YY}(\omega) \end{bmatrix},$$

such that the causal influence from X to Y is defined as:

$$f_{X\to Y}(\omega) = \ln \frac{s_{YY}(\omega)}{\tilde{h}_{YY}(\omega)\Gamma_2\tilde{h}^*_{YY}(\omega)}. \tag{2.16}$$

The interpretation of Equation (2.16) follows the same concept as Equation (2.14), such that the numerator includes intrinsic and causal power, whereas the denominator only includes the intrinsic power of series Y. Hence, if X has no causal power contributions to series Y, $f_{X\to Y} = 0$. Similarly, $f_{X\to Y}$ will increase accordingly as the influence of X on Y at frequency ω increases.

The transformations performed on the spectral MVAR model were necessary in deriving the spectral causality measures because the original transfer function, H, cannot not be decoupled into components attributable to intrinsic and causal power. The new transformations, $\overline{H}$ and $\tilde{H}$, however, contain clean terms that are easily separable into the desired quantities. Finally, a connection between the time and

frequency causal measures is given via the following set of equations:

$$F_{Y\to X} = \frac{1}{2\pi}\int_{-\pi}^{\pi} f_{Y\to X}(\omega)d\omega \qquad F_{X\to Y} = \frac{1}{2\pi}\int_{-\pi}^{\pi} f_{X\to Y}(\omega)d\omega. \tag{2.17}$$

Causal influences in both time and frequency can now be solved for, given data generated by a 2-dimensional model, and they can be verified and related through Equation (2.17). These subjects will be further explored in numerical examples in the following section, which illustrate the concepts in a more concrete manner before proceeding to the ECoG data.

2.4 Direct Causal Influences in the Frequency Domain

Granger causality can be used to measure causal influence in the spectral domain between pairs of channels. Although multi-dimension systems (such as those used in this thesis) can be reduced to a number of bivariate systems, the method selected for this research does not perform such a reduction. Thus the data from every electrode is accounted for when determining direct causal influences in the frequency domain. The function used to achieve this analysis is called the short-time direct directed transfer function (SdDTF), and it is a combination of the transfer and partial coherence functions. The transfer function was introduced in the previous section, where it was mentioned that the function measures directed influences but fails to distinguish between direct and indirect causality transference in the spectral domain.

In the case of measuring *direct* connections, partial coherence is a useful tool. Partial coherence discounts intermediate information transfer, attaining nonzero values

when the influence between channels at a particular frequency is direct. Hence, the $(i,k)^{th}$ entry of partial coherence is nonzero when channels i and k share a direct link, neglecting the influence from every other channel present in the model (Crone et al. [10]). The definition of partial coherence follows from the Spectral Matrix of series X, S_{XX} (Equation (2.12)). C is defined as S_{XX}^{-1}:

$$C(\omega) \equiv S_{XX}^{-1}(\omega) = \widehat{A}^{*}(\omega)\Sigma^{-1}\widehat{A}(\omega).$$

Then the $(i,j)^{th}$ entry of the partial coherence function, χ, at frequency ω is given by:

$$\chi_{ij}(\omega) = \frac{C_{ij}(\omega)}{\sqrt{C_{ii}(\omega)C_{jj}(\omega)}}, \tag{2.18}$$

where the subscripted ij notation is introduced, which indicates the $(i,j)^{th}$ entry of the pertinent matrix (Crone et al., [10]).

Both the transfer function and partial coherence are combined into the SdDTF, which provides a meaningful method of analyzing time series data models in the frequency domain. It is defined by Crone et al. as the normalized product of the transfer function with partial coherence so that the $(i,j)^{th}$ entry of SdDTF, ζ, at frequency ω is given by:

$$\zeta_{ij}(\omega) = \frac{|H_{ij}(\omega)||\chi_{ij}(\omega)|}{\sqrt{\sum_{\theta}\sum_{mn}|H_{mn}(\theta)|^2|\chi_{mn}(\theta)|^2}}, \tag{2.19}$$

where $\sum_{\theta}$ is the summation over all analyzed frequencies, and $\sum_{mn}$ is the summation over all combinations of unique pairs of channels. A nonzero $(i,j)^{th}$ entry of ζ at frequency ω indicates a direct causal flow from channel j to channel i at frequency

ω, thus the function conceptually combines the notions of the transfer function and partial coherence (Crone et al., [10]).

One remaining issue to address is the method of analyzing the SdDTF results. Typically, grids of time-frequency plots (time along x-axis and frequency along the y-axis) are generated to illustrate the causal flow between channels, with the plot located at the $(i, j)^{th}$ position of the grid (row i, column j) indicating the flow of the modeled data from channel i to the modeled data from channel j. Drawing meaningful conclusions from grids of the dimensions contained in Table 2.1 of time-frequency plots would be cumbersome, as the data sets are so rich due to the large number of electrodes used per patient. Therefore, this thesis characterizes each time-frequency plot by the *maximum* SdDTF value obtained across the entire time and frequency domains.

Once the grids of SdDTF maximum plots were constructed, connectivity between anatomical locations was further examined by generating graphs whose nodes represent anatomical locations and edge widths represent the maximum SdDTF values across time and frequency (graphs were plotted with Matlab's Bioinformatics Toolbox). The causal influences occurring in high gamma frequencies were thus transformed into graphical representations, providing a novel method of visualizing the mechanisms underlying speech production during Wordstem.

Numerical examples were implemented to illustrate the concepts of causality, from Granger to the SdDTF. The first example is a bivariate model replicated from section

17.5 of Ding et al. [6]. For both simulations, the time series data were generated for 500 time points for 50 trials. The 2 node model was generated from equations:

$$X(t) = 0.9X(t-1) - 0.5X(t-2) + \varepsilon(t)$$

$$Y(t) = 0.8Y(t-1) - 0.5Y(t-2) + 0.16X(t-1) - 0.2X(t-2) + \eta(t),$$

where $\varepsilon(t)$ and $\eta(t)$ are random Gaussian, zero mean error terms with variances $\sigma_1^2 = 1$ and $\sigma_2^2 = 0.7$, respectively, and covariance 0.4. These values yield a covariance matrix of:

$$\Sigma = \begin{bmatrix} 1 & 0.4 \\ 0.4 & 0.7 \end{bmatrix}.$$

Using the AIC model order given by the `cca_find_model_order_mtrial` function of the GCCA toolbox, the MVAR models were solved for using the `armorf` function of the same toolbox for dimension 1 (treating each series separately, as in Equations (2.5) and (2.6)) and dimension 2 (as in Equation (2.7)). For the 2-dimensional system, the correct model order of the time series equations is 2, which both the AIC and BIC correctly solved for via Equations (2.3) and (2.4), as shown in Figure 2.4 .

First, the causal influences were calculated according to Equations (2.9) and (2.10), and upon one simulation of 50 trials, these values were:

$$F_{X\to Y} = 0.0506 \qquad F_{Y\to X} = 1.3960 \times 10^{-4}$$

These value indicate that upon increasing the dimension of the system, the error from the 1-dimensional MVAR model for Y decreased with the addition of series X to the

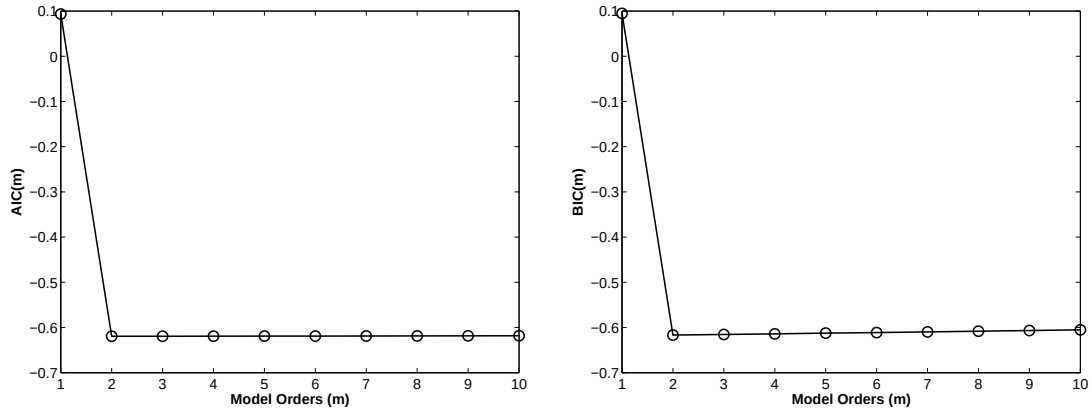

(a) AIC values for the 2 node example (b) BIC values for the 2 node example

Figure 2.4 : AIC and BIC values for the 2 node model.

model, hence X has a causal influence on Y. Alternatively, incorporating data from Y into the MVAR model for X had little impact on decreasing the error, indicating that Y has less of a causal influence on X. These results are in line with time series equations used to generate the data.

Causality in the frequency domain was then calculated via Equations (2.16) and (2.14) for $\omega \in [0, \pi]$, from which Figure 2.5 was created. The plot of $f_{X \to Y}$ in Figure 2.5 indicates greater influence from Node X to Node Y, whereas the values $f_{X \to Y}$ show quite the opposite effect of Node Y on Node X, again in agreement with the time series equations used to generate this model.

The magnitudes of transfer function values were calculated for the 2 node example using Equation (2.11), and the results are shown in Figure 2.6. The x-axis is labeled in time, which refers to the period covered in the calculation. In this model, the transfer

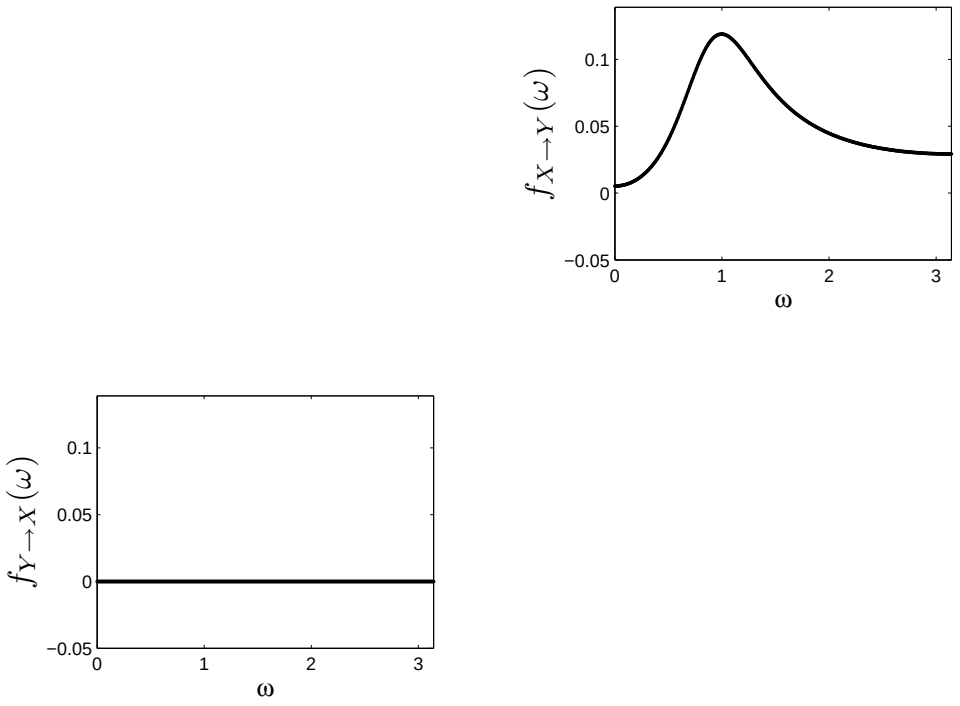

Figure 2.5 : Causal influence in the frequency domain for 2 node model calculated from Equations (2.14) and (2.16). These plots align with the dependencies in the time series equations used to generate the model.

function does not vary with time; however, the function values can vary with longer time domains, so the time axis remains in keeping with convention. Letting Channel 1 refer to Node X and Channel 2 refer to Node Y, the nonzero transfer function values in plot $|H_{21}|$ confirm the transference from Node X to Node Y at the frequencies indicated in Figure 2.5, whereas the $|H_{12}|$ illustrates how little "information" is transferred to Node Y to Node X over the entire spectral domain.

The simplicity of the 2 node example fails to illustrate the concepts of transfer function discussed previously, so a 3 node example, which includes intermediate

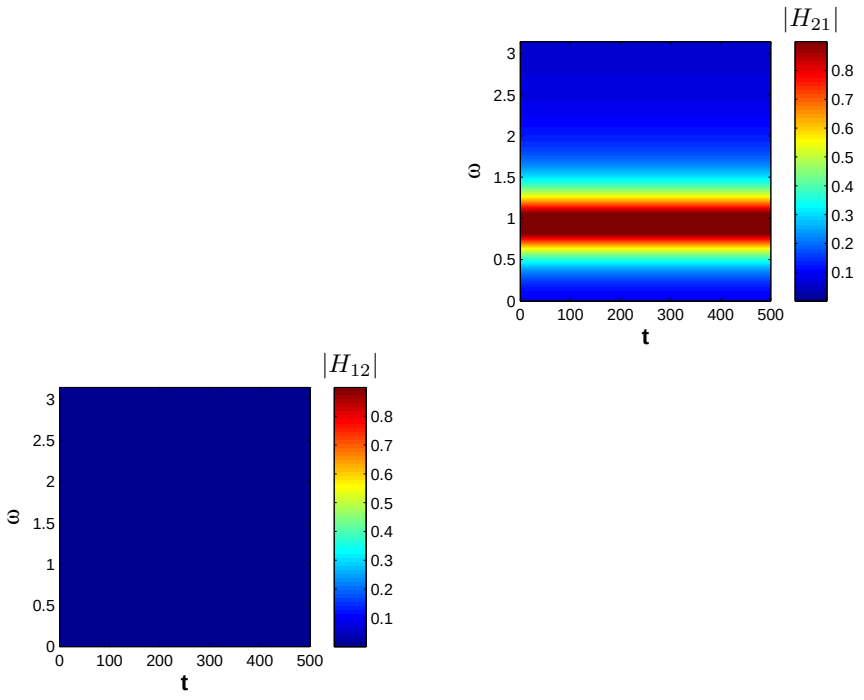

Figure 2.6 : Transfer function values for 2 node model calculated from Equation (2.11). The time axis refers to the total range covered in the calculation; for this case, the transfer function is uniform across time and varies with frequency. In accord with the time series equations, the nonzero transfer function values in the $|H_{21}|$ block of this figure indicate signal transference from Node X to Node Y, whereas the values much less in magnitude in the $|H_{12}|$ block verify the lack of signal transference from Node Y to Node X.

transference, is now introduced. The time series equations for this example are:

$$X(t) = 0.9X(t-1) - 0.5X(t-1) + \varepsilon(t)$$

$$Y(t) = 0.3Y(t-1) - 0.4Y(t-2) + 0.7X(t-1) - 0.8X(t-2) + \eta(t)$$

$$Z(t) = 0.8Y(t-1) + 0.5Z(t-2) + \gamma(t),$$

where the covariance matrix is:

$$\Sigma = \begin{bmatrix} 1 & 0 & 0 \\ 0 & 0.5 & 0 \\ 0 & 0 & 0.6 \end{bmatrix}.$$

This example does not include any cross-covariance terms, and $\varepsilon(t)$, $\eta(t)$, and $\gamma(t)$ are random Gaussian terms with zero means and variances provided in the diagonal entries of Σ. Beginning with the transfer function for the 3 node model, Figure 2.7 illustrates the nonzero values in the $|H_{31}|$ block, indicating transference from Channel 1 (Node X in the time series equations) to Channel 3 (Node Z). However, as depicted in the schematic of Figure 2.3 (which reflects the time dependencies of this example), Channel 1 is not directly transmitting data to Channel 3. If the interests are in capturing direct connectivity, partial coherence values need to be considered in addition to the transfer function values, as is the case with the SdDTF.

The magnitudes of partial coherence values were calculated using Equation (2.18) for both the 2 and 3 node examples, where nonzero values indicate direct connections. In the 2 node case shown in Figure 2.8, both nodes share a link, which is reflected in the nonzero function values in both $|\chi_{12}|$ and $|\chi_{21}|$ plots (note that partial coherence is symmetric).

The partial coherence plots for the 3 node example are shown in Figure 2.9, which further illustrates the concept of intermediate vs. direct connectivity. The values of

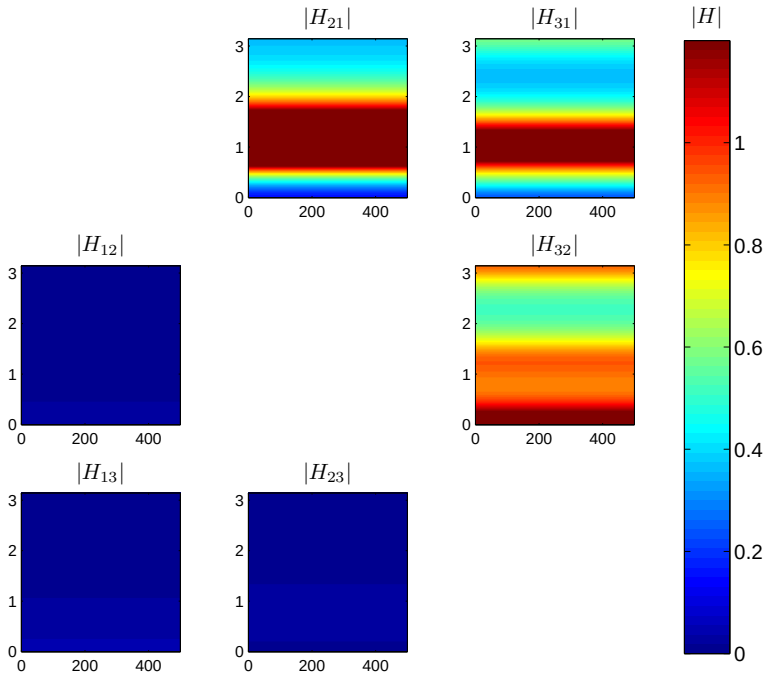

Figure 2.7 : Transfer function values for 3 node model calculated from Equation (2.11). In this example, the function is constant across time, varying only across frequency. In accord with the time series equations, the nonzero transfer function values in the $|H_{21}|$ and $|H_{32}|$ plots indicate the appropriate signal transfers from Channel 1 to Channel 2 and Channel 2 to Channel 3, respectively. However, the nonzero values of plot $|H_{31}|$ plot show that the transfer function does not distinguish the indirect connection from Channel 1 to Channel 3.

the $|\chi_{31}|$ and $|\chi_{13}|$ plots signify that Channels 1 and 3 are not directly linked to each other, which is the case for this example.

Finally, the transfer function and partial coherence were combined into the SdDTF calculations, in which Equation (2.19) was used to calculate direct signal transference

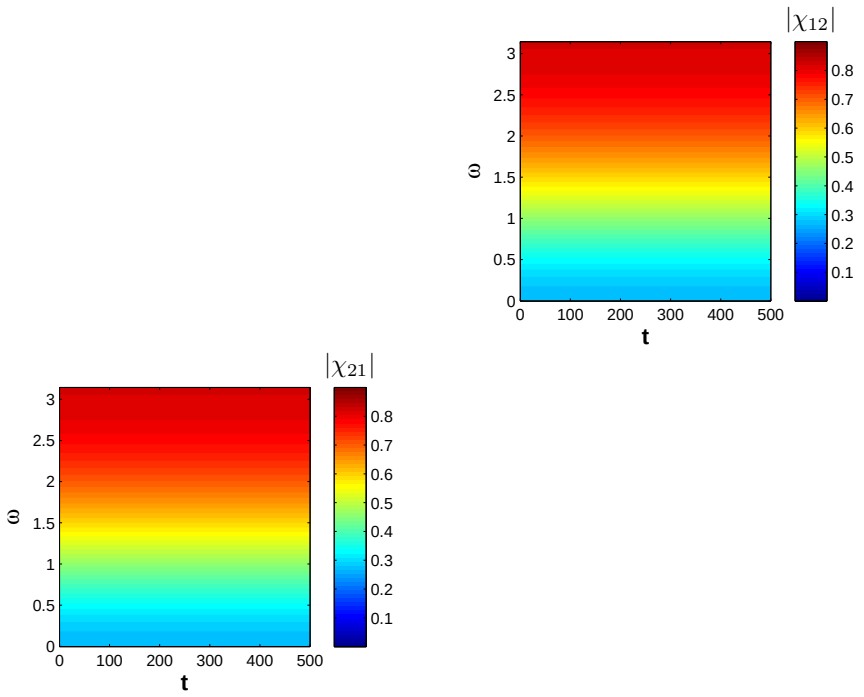

Figure 2.8 : Partial coherence for 2 node model calculated from Equation (2.18). As with the transfer function, partial coherence only varies with frequency for this example, where the time axis refers to the total range covered in the calculation. The nonzero function values in both plots indicate the direct connectivity of Channels 1 and 2, which is indeed the case.

across the entire frequency domain. The SdDTF values for the 2 node model in the ζ_{21} block of Figure 2.10 are in accord with the both the numerical model and the frequency values which correspond to the increasing $f_{X\to Y}$ values in Figure 2.5.

The SdDTF values for the 3 node model are shown in Figure 2.11, which are line with Node X transmitting information to Node Y, which, in turn, transmits information to Node Z. The SdDTF is a means of "summarizing" and thus capturing the

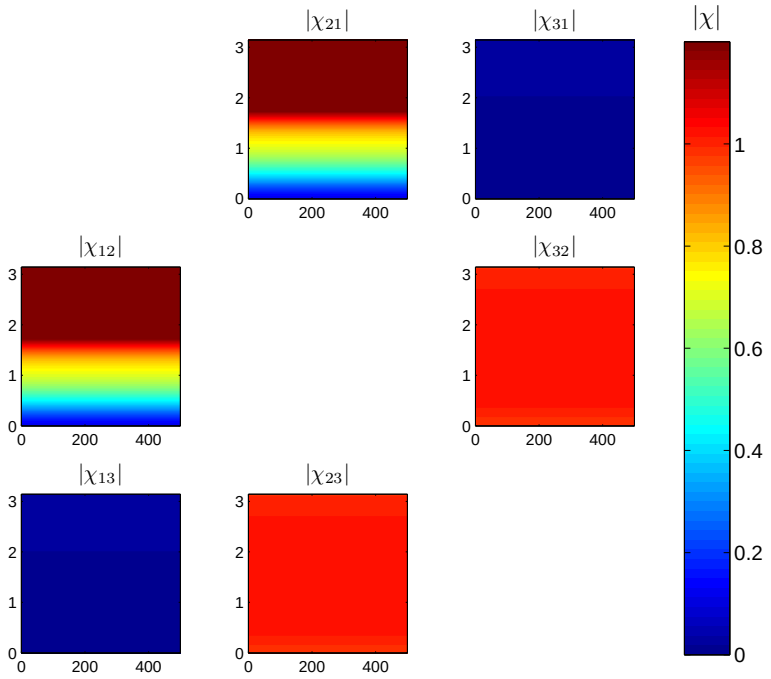

Figure 2.9 : Partial coherence for 3 node model calculated from Equation (2.18). In agreement with the time series equations, the function values in the 13 and 31 blocks indicate that these channels are not directly connected, whereas the values in blocks 23, 32, 12, and 21 signify that Channels 1 and 2 are connected, as well as Channels 2 and 3.

causal dynamics of the system, including direct connectivity and directed information transmission across the frequency domain desired for analysis.

As previously mentioned, the SdDTF results are typically displayed in grids of time-frequency plots (such as in Figures 2.10 and 2.11) which illustrate the direct influences present between the channels. As these were 2- and 3-dimensional systems, any variability is easily distinguished; however, as the number of channels (corre-

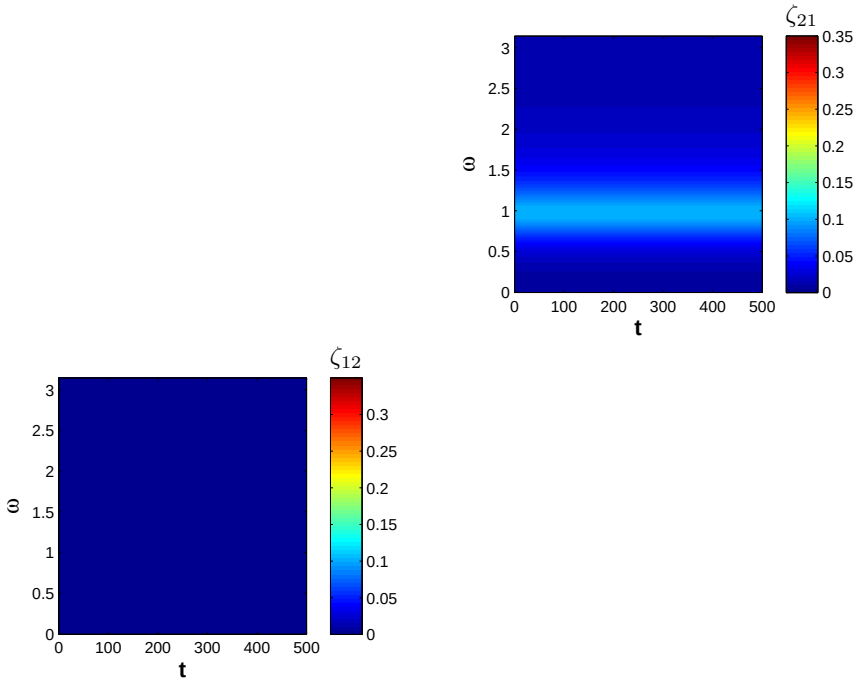

Figure 2.10 : SdDTF for 2 node model calculated from Equation (2.19). Again, the time axis refers to the total range covered in the calculation, where, for this case, the SdDTF is uniform across time and varies with frequency. The SdDTF results indicate direct transference from Node X to Node Y, as noted in the ζ_{21} plot, as well as a lack of direct signal transference in the opposite direction, as seen in the ζ_{12} plot.

sponding to the dimension of the system) increases, the finer details of each plot of the grid may be lost. In order to simplify the analysis of the ECoG data, each block of SdDTF values of the grid was defined by the maximum value attained. For instance, by defining each plot in Figure 2.10 by its maximum ζ value, Figure 2.12 was created (this resulting function is denoted $\overline{\zeta}$). Simplifying the data across the frequency domain (and the time domain, if applicable) in this manner allows for the

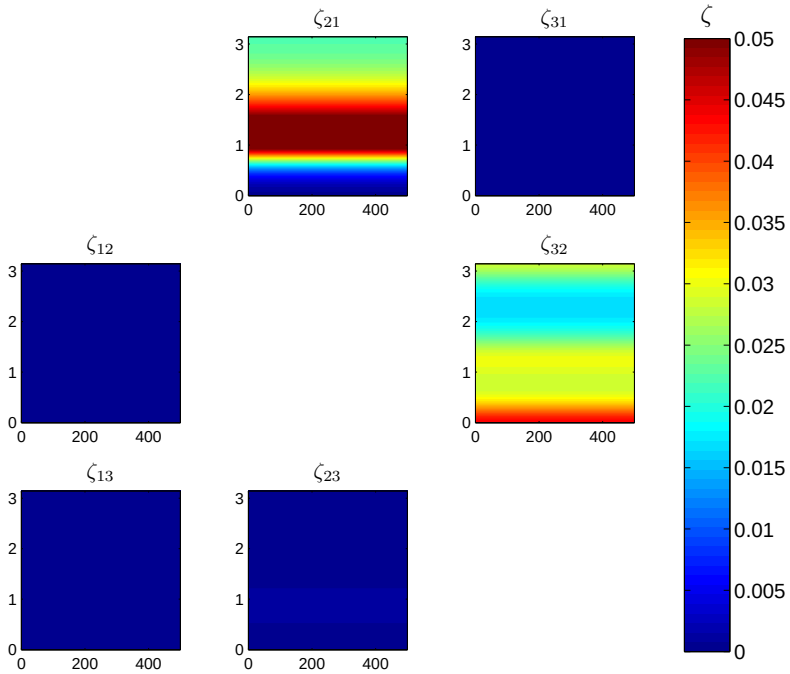

Figure 2.11 : SdDTF for 3 node model calculated from Equation (2.19). Again, the time axis refers to the total range covered in the calculation, where, for this case, the SdDTF is uniform across time and varies with frequency. The SdDTF results indicate direct transference from Node X to Node Y and from Node Y to Node Z, as noted in the ζ_{21} and ζ_{32} plots.

compression of complex data sets, such as the higher dimensional ECoG time series data recordings. Additionally, by compressing this data, further graphical analysis can be performed in which the nodes of the graph represent anatomical locations of the original channels that generated the time series data and the edge widths are proportional to the $\overline{\zeta}$ values.

By treating the matrix of maximum SdDTF values as an adjacency matrix, the

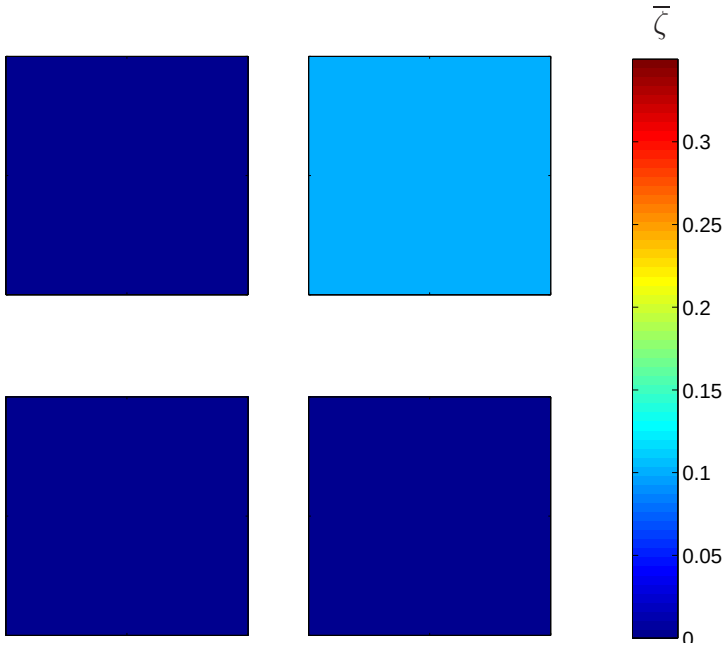

Figure 2.12 : Each block in this figure was obtained by taking the maximum SdDTF value in the corresponding block of Figure 2.10 (the resulting function is denoted $\overline{\zeta}$). This characterization compresses the data across the frequency domain, and had the data varied across time, this calculation would have compressed along the time domain as well. This "reduction of information" allows one to view the entire system in a simplified way, an important factor given the complexity of the ECoG data sets for each subject.

graph in Figure 2.13 was constructed, where the edge widths are proportional to the values used to generate Figure 2.12. These examples, albeit trivial, illustrate the reasoning behind the methodology executed in this research. They bridge the connection from causal influence in time (Equations (2.9) and (2.10)), to causal influence in the spectral domain (Equations (2.14) and (2.16)), to a measure of direct causal influ-

ence in the frequency domain (Equation (2.19)), and finally to a graphical model that summarizes direct causal influence across all time and frequencies. The figures generated serve as testaments to the human ECoG data analysis. If the time series data were generated by human ECoG recordings during a language task, the nodes of the graph contained in Figure 2.13 would indicate that the anatomical region underneath Channel 1 were having a insignificant causal influence on the region underneath the Channel 2. Such results would be indicative of the relevance of specific brain regions to the process of word production, which is the heart of language research.

Figure 2.13 : This graph was generated by treating the $\overline{\zeta}$ values used to create Figure 2.12 as an adjacency matrix. The edge widths are proportional to the $\overline{\zeta}$ values, indicating the influence that Node X has on Node Y versus the lack of influence that Node Y has on Node X in the frequency domain.

Having established the methods to be implemented, the next steps are executing

them and analyzing the results; however, one final issue must be addressed prior to implementation. Equations (2.11), (2.18), and (2.19) rely upon the MVAR model of the time series data, which was developed based on initial assumptions. If the time series data do not meet these assumptions, the results lose meaning and validity. Preprocessing, discussed in the following section, is a means of achieving these initial assumptions and is therefore a crucial stage of implementation.

2.5 Processing the ECoG Data Prior to Analysis

The very foundation of SdDTF relies on the initial assumptions that the data has zero mean and is autocorrelation ergodic. Figure 2.2 at the beginning of Chapter 2 illustrates the lack of stationarity across trial averages in the empirical data. Thus, *preprocessing* is an essential stage of analysis, i.e., changes must be made to the data to ensure that it meets the initial assumptions, which are necessary when solving each MVAR model.

Two methods of preprocessing were followed for this research. Method 1 follows Ding et al.'s 2000 paper and consisted of applying the following steps to the data from each channel:

1. Preprocessing Method 1
    (a) Linearly detrend each trial
    (b) On every trial, subtract the temporal mean and divide by the temporal standard deviation

(c) At every time point, subtract the trial mean and divide by the trial standard deviation

(d) Cover each trial with short, highly overlapping windows

The final step is applied to remove the "deeper source of nonstationarity" present in the "correlation structure in the data" (Ding et al., [5]). Upon "windowing" the data, MVAR models were then solved for on each short epoch, a technique referred to as Adaptive Multivariate Autoregressive (AMVAR) modeling. Hence, the resulting "AMVAR procedure yields finely resolved dynamical information about the cortical processes related to cognitive state" (Ding et al., [5]). Mullen points out the importance of performing step 1(b) prior to step 1(c) when implementing AMVAR over short time windows to ensure that "all variables will have equal weight (variance) across the trial" [14].

Preprocessing Method 2 applied the windowing step earlier in the analysis, following a suggestion made by Seth, and consisted of following the steps below for the data from each channel [19]:

1. Preprocessing Method 2

   (a) Linearly detrend each trial

   (b) At every time point, subtract the trial mean and divide by the trial standard deviation

   (c) Cover each trial with short, highly overlapping windows

(d) Across every window, subtract the temporal mean and divide by the temporal standard deviation

Crone et al. perform Method 2 with the exception of linearly detrending each trial, but Ding et al. recommend both steps 1(a) and 1(b) (equivalently, 2(a) and 2(d)) to ensure that the resulting "data from each channel and each trial were given equal weight in model estimation" (Crone et al, [10], [11]; Ding et al., [5]). However, Ding et al. warn against the removal of temporal mean and division by temporal standard deviation over too short of a duration of time, as the temporal mean will be more variable and subtracting it will incorrectly alter the analysis in the frequency domain. The example used to support this claim was 10 points in duration; elsewhere, "short" is not explicitly defined (Ding et al. [5]). It was because of this suggestion that Preprocessing Method 1 was implemented.

Following the preprocessing of the ECoG data, the functions presented in Chapter 2 were solved for to determine key regions in the process of speech production. Additional details concerning implementation are the topic of the following section.

2.6 Practical Application of Theory to ECoG Data

Following data processing and exportation into Matlab, selection of the final sets of electrodes and trials, and identification of the epoch of time for analysis, the time series data were preprocessed following the two methods covered in Section 2.4. Both preprocessing approaches implement windowing and thus require knowledge of win-

dow length. Ding et al. combine prior knowledge and experimental results with plots of cross correlations at several window lengths to select the duration that captures variability while still allowing the data to be treated as locally stationary [5]. Crone et al. used a window length of 360 ms (120 samples) with a 15 ms (5 sample) shift in their 2008 and 2011 ECoG papers, and they use the following "rule of thumb" when selecting the window length:

$$\frac{K(p+1)}{N_s n_t} < 0.1 \tag{2.20}$$

where K is the number of channels, p is the model order, N_s is the window length, and n_t is the number of trials [10]. Mullen also recommends adhering to the above criteria when selecting the window length [14].

Equation (2.20) relies upon the window length and the model order, whereas the model order cannot be determined without the window length (note the circular logic). The window length used in this research incorporated Equation (2.20) with the frequencies that the length would allow for analysis, as high gamma frequencies were of ultimate interest for this study. In the end, both preprocessing methods were implemented with window lengths of 300 ms and a 15 ms shift. In the end, each trial was subdivided into overlapping time windows such that the first point of each window was shifted forward 15 ms until the entire epoch was covered. The values for both preprocessing methods for Equation (2.20) are displayed in Table 2.2, which shows that with this window length, the data from each patient adhered the "rule of thumb." Table 2.2 subdivides the parameter values according to AIC and BIC

columns because, as will be described shortly, the MVAR models were solved for using model orders given by both criteria.

	Preprocessing Method 1		Preprocessing Method 2	
Patient ID	AIC	BIC	AIC	BIC
ta355	0.06147	0.02332	0.06417	0.02332
ta356	0.05624	0.01875	0.06218	0.02343
ta401	0.06569	0.02628	0.07795	0.02628
ta408	0.06271	0.01943	0.05052	0.01736
ta439	0.05124	0.02050	0.05227	0.02050
ta442	0.04925	0.02716	0.05657	0.02716
ta451	0.05183	0.01876	0.05644	0.01923

Table 2.2 : $\frac{K(p+1)}{N_s n_t}$ values for 300 ms window length

The AMVAR models were then solved for over a range of orders within each window in order to determine the AIC and BIC values. The window shift was adjusted to save computation time when calculating the model orders on each window across the entire time domain. For AIC, the shift was increased to 50 ms, and for BIC the shift was increased 100 ms (note that even with these increases, these computations took several days to complete). Then, the next integer greater than the average of the criteria (or the ceiling of the average) over all windows was used as the global model

order for all windows. This process was repeated for all patients, and the results are presented in the Table 2.3 below. The AMVAR models were recalculated for the final

	Preprocessing Method 1		Preprocessing Method 2	
Patient ID	AIC	BIC	AIC	BIC
ta355	10	3	10	3
ta356	11	3	13	4
ta401	9	3	11	3
ta408	16	4	12	2
ta439	9	3	10	3
ta442	7	3	8	3
ta451	11	3	12	4

Table 2.3 : AIC and BIC values calculated from Equations (2.3) and (2.4) for all patients used in this study. The values were found on a range of orders across windows that covered the entire trial, and the next integer larger than the average over all windows was calculated to determine the values of this table, which were ultimately used as the global model order for each window upon implementation.

implementation on each window using the model orders in Table 2.3. The technique of using the same model order for each window is in line with Crone et al. and Ding et al.'s works ([10], [11], and [5]). It was from these orders that the values in Equation

(2.20) were calculated.

Upon determining the model orders, Equation (2.2) was solved in each window. When I initially solved Equation (2.2) for the coefficient matrices, I used the following formula combined with definition (1.4) to construct each $\tilde{R}_{XX}(\cdot)$ (the tilde notation signifies empirical data):

$$\tilde{R}_{XX}(n) = \frac{1}{N-n} \sum_{t=1}^{N-n} \tilde{X}(t)\tilde{X}^*(t+n) \tag{2.21}$$

where N is the total number of time points per window, and each $\tilde{R}_{XX}(\cdot)$ is averaged over trials (found in Table 2.1) (Crone et al., [10] and [11], Ding et al., [6] and [5]). I proceeded to solve for the coefficients matrices "directly," that is, I used Equation (2.21) to build the Yule-Walker Equations given in Equation (2.2) and subsequently solved for the unknown convolution coefficient matrices. To compute the SdDTF, Σ must be found, and I used the representation derived next.

Beginning with Equation (2.1):

$$\varepsilon(t) = X(t) + \sum_{j=1}^{p} A(j)X(t-j).$$

With $A(0) = Id(n)$, the $n \times n$ identity matrix, the summation index starts at 0:

$$\varepsilon(t) = \sum_{j=0}^{p} A(j)X(t-j).$$

Right multiply by $\varepsilon^*(t)$, take expectations, and distribute $E[\cdot]$:

$$E\left[\varepsilon(t)\varepsilon^*(t)\right] = \sum_{j=0}^{p} A(j)E\left[X(t-j)\varepsilon^*(t)\right],$$

but $E[X(t-j)\varepsilon^*(t)] = 0$ for $j > 0$, which leaves:

$$E\left[\varepsilon(t)\varepsilon^*(t)\right] = A(0)E\left[X(t)\varepsilon^*(t)\right].$$

As $A(0) = Id(n)$ and using the definition for $\varepsilon^*(t)$, the equation becomes:

$$E\left[\varepsilon(t)\varepsilon^*(t)\right] = E\left[X(t)\left(\sum_{k=0}^{p} A(k)X(t-k)\right)^*\right];$$

apply transposition, move the summation outside $E[\cdot]$, and distribute $E[\cdot]$ to obtain:

$$E\left[\varepsilon(t)\varepsilon^*(t)\right] = \sum_{k=0}^{p} E\left[X(t)X^*(t-k)\right]A^*(k).$$

Use Definition (1.4):

$$E\left[\varepsilon(t)\varepsilon^*(t)\right] = \sum_{k=0}^{p} R_{XX}(-k)A^*(k).$$

The combined results yield:

$$\Sigma = E\left[\varepsilon(t)\varepsilon^*(t)\right] = \sum_{k=0}^{p} R_{XX}(-k)A^*(k).$$

Using "modified" symmetry of the time-lag dependent correlation matrices from equation (1.4) and symmetry of the covariance matrix Σ, take the transpose of both sides of the equation to obtain an explicit formula for Σ (note covariance matrices are equivalent to correlation matrices due to zero mean):

$$\Sigma = \sum_{k=0}^{p} A(k)R_{XX}(k). \tag{2.22}$$

After using Equation (2.22) to solve for Σ in each window, I began calculating the SdDTF values for synthetically-generated data (specifically the 2 node example). The

implementation seemed to be successful, as the correct model orders were solved for from the simulated. Additionally, SdDTF results similar to those in Figure 2.10 were generated. However, this method failed when applied to ECoG data, as was evident in covariance matrices Σ with negative determinants, indicating that the covariances matrices became non- positive definite.

It was because of this setback that the `armorf.m` function in the Matlab GCCA Toolbox was substituted to construct both the coefficient matrices and Σ. This function implements Morf's method to determine these variables (Seth, [19]). Once this function was used to calculate the model orders and MVAR models on each window, the analysis continued by extending the computations into the frequency domain.

For discrete time points defined as $t_k = kh$, where $h = dt = 1\,\text{ms}$, $k = 0, \ldots, N-1$ and $t_{N-1} = 300\,\text{ms}$ (equivalently the final point of each window), the discrete frequency step was calculated via (section 7.4, [4]):

$$d\omega = \frac{1}{Nh},$$

from which the discrete frequency samples were calculated:

$$\omega_k = kd\omega, \quad k = 0, \ldots, N-1.$$

The domain was restricted to $60-150\,\text{Hz}$ to encompass mid to high gamma frequencies without exceeding the Nyquist frequency on each 300 ms window. Combining this discretization with the coefficient matrices and Σ, the transfer function H, partial coherence χ, and the SdDTF values ζ, were solved for using Equations (2.11), (2.18),

and (2.19). Hence, the SdDTF values were calculated every 15 ms across each 300 ms window over the $60 - 150$ Hz frequency range. Thus the implemented procedure was:

1. Define 300 ms window
2. Calculate MVAR on window
3. Calculate SdDTF on window
4. Shift window forward 15 ms
5. If reached the end of entire trial, exit; else return to step 1

From these SdDTF values, the $\overline{\zeta}$ values were calculated, from which graphical models were generated. All of the results will be discussed in the next section, where further motivation for using $\overline{\zeta}$ is presented in the context of the ECoG data and comparisons to results of speech models are made.

Chapter 3

Results

3.1 Causal Influence Results from ECoG Data

Using the techniques presented in Chapter 2, the time series data recorded from intracranial electrodes during the Wordstem language task was exported into Matlab, preprocessed, and analyzed. In line with other ECoG studies, the goal of this research was to determine causal influences occurring between brain regions in high gamma frequencies during speech production. The Wordstem task is unique in that subjects are neither repeating words nor responding to picture stimuli. This task required subjects to generate complete words from incomplete word fragments, introducing an element not present in other ECoG studies researched (Crone et al. [10], [11]; Edwards et al. [7]).

Analyzing ECoG data sets is a complicated endeavor, regardless of the task during which the recordings are taken. This research began by following the path set by Crone et al. by calculating the SdDTF values over highly overlapping windows (300 ms long windows with a 15 ms shift) that spanned the pre-stimulus to post-articulation epoch over all trials for each patient. After channels with epileptiform activity and/or 60 Hz noise were excluded, the data from the remaining electrodes

was used to solve for the AMVAR model in each window. Mullen recommends using as many channels as possible, as opposed to including data from a subset of electrodes [14]. Choosing to include all channels introduced challenges that prompted simplifications in the analysis.

The first simplification made was due to the number of electrodes, which corresponds to the dimension of the AMVAR models in the overlapping windows (see Table 2.1). Because of the large number of electrodes implanted per patient relative to other ECoG studies, the time-frequency graphs (such as the one in Figure 2.10 for the 2 node model) were not created. Rather, the maximum SdDTF matrices were solved for directly (recall Figure 2.12), thus compressing time and frequency domains. As the SdDTF values were originally restricted to $60 - 150\,\text{Hz}$, these results still pertain to the high gamma frequency range.

The second simplification in the analysis was made after the plots of the SdDTF maximum matrices (denoted $\overline{\zeta}$) were generated for each patient. Recall that each pixel in these images represents the maximum SdDTF value attained across time and frequency between a pair of electrodes. Figure 3.1 illustrates one such matrix (recall Figure 2.12 from the 2 node model presented in Section 2.4).

Following the same procedures outlined in the examples in Section 2.4, the matrices of SdDTF maximum values were treated as adjacency matrices so that the nodes and edges of the resulting graphs displayed directionality and (proportional) magnitude of direct, directed causal influences. Most entries of these matrices are

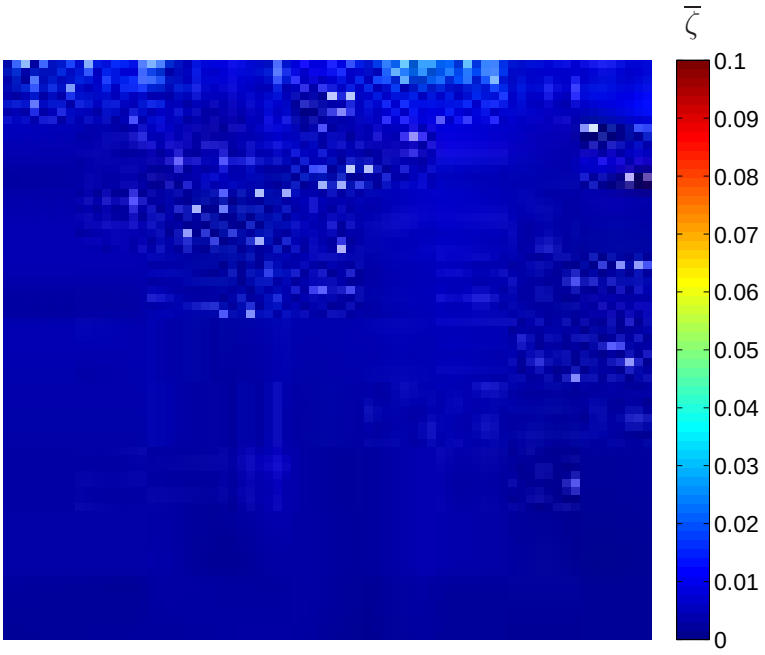

Figure 3.1 : 72×72 matrix of SdDTF maximum values where each pixel represents the maximum SdDTF value reached across time and frequency between two electrodes.

nonzero, so thresholds were introduced to include only entries greater than a certain magnitude. When $\overline{\zeta}$ values exceeding a subjective threshold of 0.03 were retained from the matrix shown in Figure 3.1, the graph in Figure 3.2 was created (using Matlab's Bioinformatics Toolbox).

This graph (and any others similarly generated) would need to be decoded for every patient to gain intuition about its meaning. The colors of each node represent anatomical regions, and the numbers represent electrode numbers assigned after implantation. Electrodes were not implanted in the exact same anatomical locations for each patient, so the numberings are patient-specific. This inconsistency in the labels posed a challenge in drawing cross-patient comparisons and global conclusions, given

that so many electrodes were implanted in all seven patients.

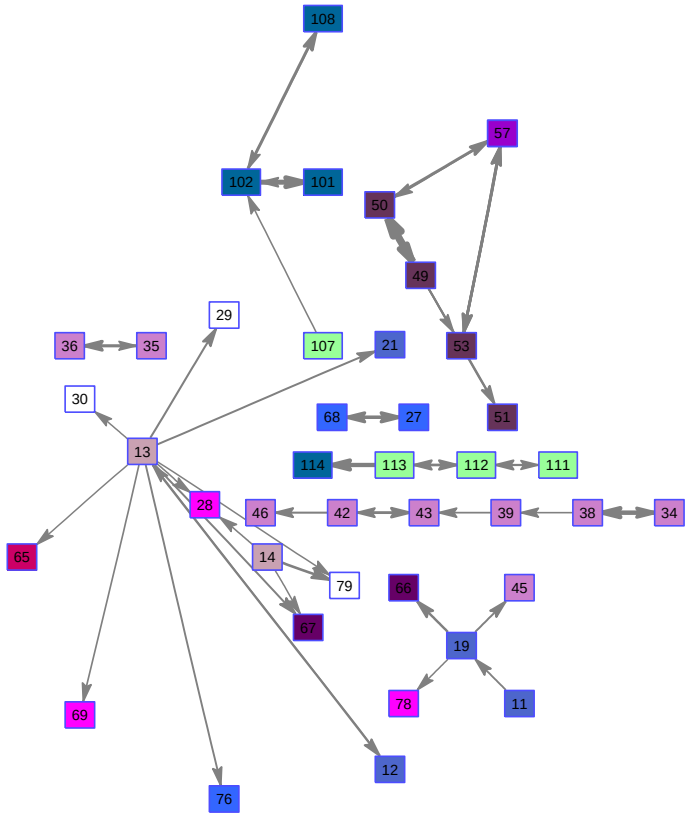

Figure 3.2 : Graph generated after retaining values above a threshold of 0.03 from the adjacency matrix in Figure 3.1 . The colors of each node indicate anatomical regions. The number labels of each node correspond to post-surgical labeling conventions and are patient-specific.

When the ECoG data is exported into Matlab, an identifier is assigned to each electrode that classifies its implantation site based on broader, pre-defined anatomical regions common to most human brains (and all patients used in this study). Rather than analyzing the results based on electrode locations, the activity from each of these

wider regions was accumulated from all patients and averaged.

Finally, only a subset of regions in the left hemisphere was used for the graphical illustrations (although data from all electrodes was used when constructing the AMVAR models). The regions used for the graphs (and the cumulative number of electrodes that contributed ECoG data per area) are shown in Figure 3.3, where each color indicates a different region.

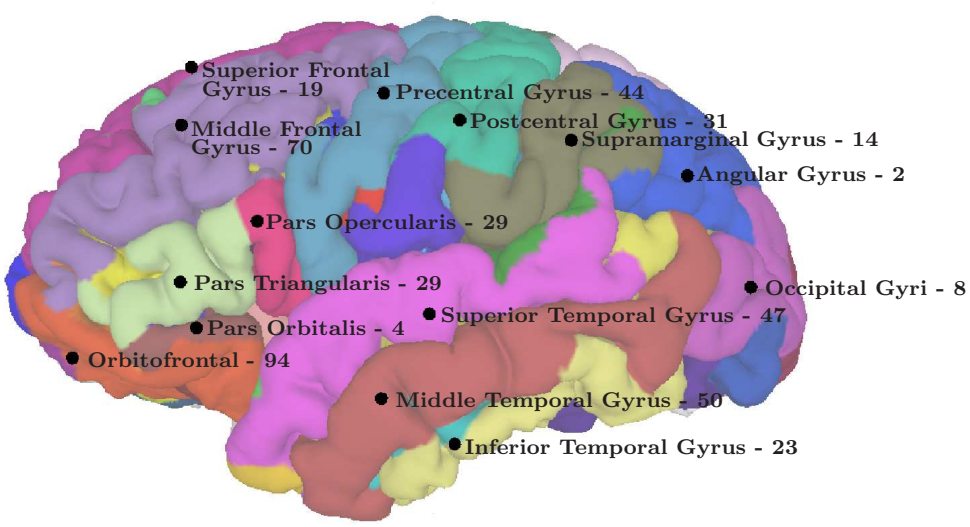

Figure 3.3 : The anatomical locations in the left hemisphere of the brain selected for the SdDTF causal influence analysis. Included are the summed electrode counts from all patients.

Using these anatomical regions, the maximum SdDTF matrices were solved for each patient (recall Figure 3.1), accumulated, and then grouped by the regions in Figure 3.3. Denote this cumulative matrix $\hat{\zeta}$, where entry $\hat{\zeta}(i,j)$ reprents the maxi-

mum SdDTF value from region i to region j summed over all patients. As Figure 3.3 indicates, the electrodes are not evenly distributed in each region, so the entries of $\hat{\zeta}$ were averaged by electrodes. For example, entry $\hat{\zeta}(i,j)$ was divided by the $N_i + N_j$, where the data was modeled from a total of N_i electrodes implanted in the region represented by row i and N_j electrodes implanted in the region represented by column j. This process was repeated for all combinations of preprocessing methods and AMVAR model orders dictated by the AIC or BIC. These electrode-averaged matrices are given in Figures 3.4, 3.5, 3.6, and 3.7.

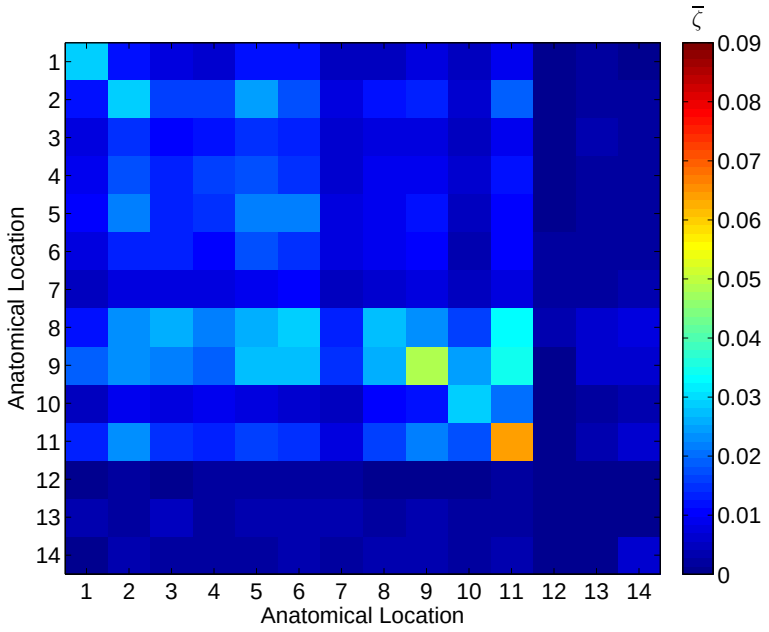

Figure 3.4 : Electrode averaged matrix of regional maximum SdDTF values solved for from ECoG data preprocessed using Preprocessing Method 1 and AMVAR models using orders given by the AIC.

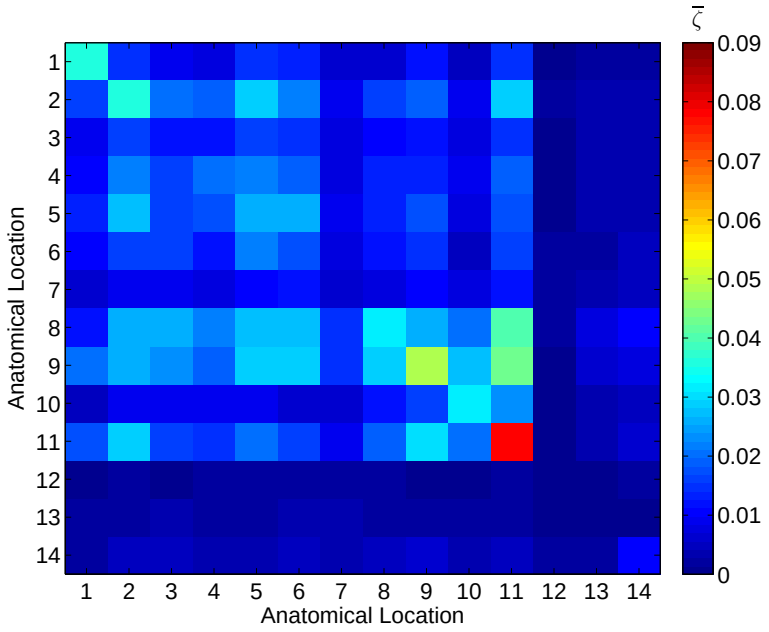

Figure 3.5 : Electrode averaged matrix of regional maximum SdDTF values solved for from ECoG data preprocessed using Preprocessing Method 2 and AMVAR models using orders given by the AIC.

In order to enhance the visualizations of the results, the matrices were treated as adjacency matrices and graphed on a background image of a brain. The nodes are strategically positioned in the appropriate regions, and the edge widths are proportional to the electrode averaged $\hat{\zeta}$ values. The four graphs generated from the matrices in Figures 3.4, 3.5, 3.6, and 3.7 are shown in Figures 3.8, 3.9, 3.10, and 3.11, respectively.

Sites in the temporal and frontal gyri, and the motor cortex are consistently implicated in modern studies as having significant roles during speech production.

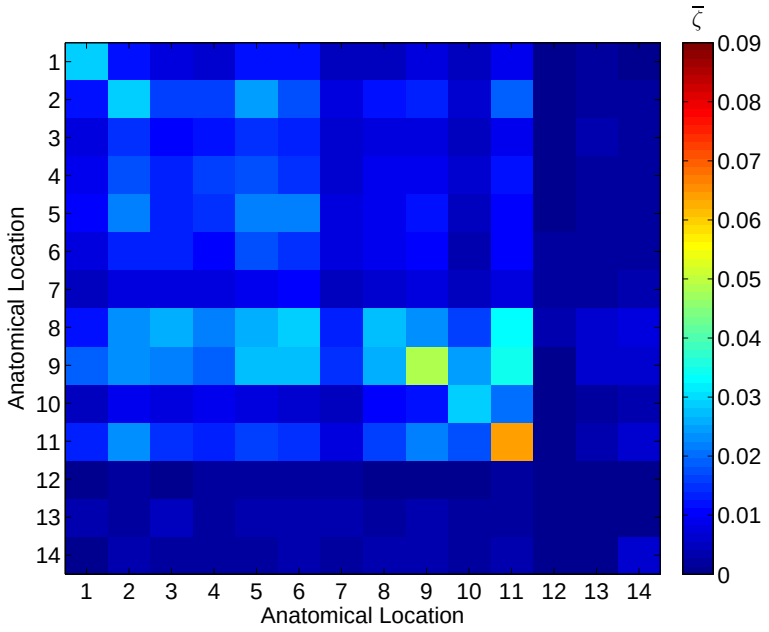

Figure 3.6 : Electrode averaged matrix of regional maximum SdDTF values solved for from ECoG data preprocessed using Preprocessing Method 1 and AMVAR models using orders given by the BIC.

The edges flowing in and out of the superior and middle temporal gyri, the middle frontal gyrus, the orbitofrontal cortex, and the pre and postcentral gyrus are greater in thickness than other edges (from Figures 3.8, 3.9, 3.10, and 3.11). Hence, these results from the analysis introduced in this research do not contradict findings from ECoG and imaging studies that claim that these same areas are involved in language production. (Crone et al. [11]; Indefrey and Levelt [8]).

In depth comparisons to results from modern studies are difficult for two reasons. First, as the method implemented in this study is new, no other results exist for com-

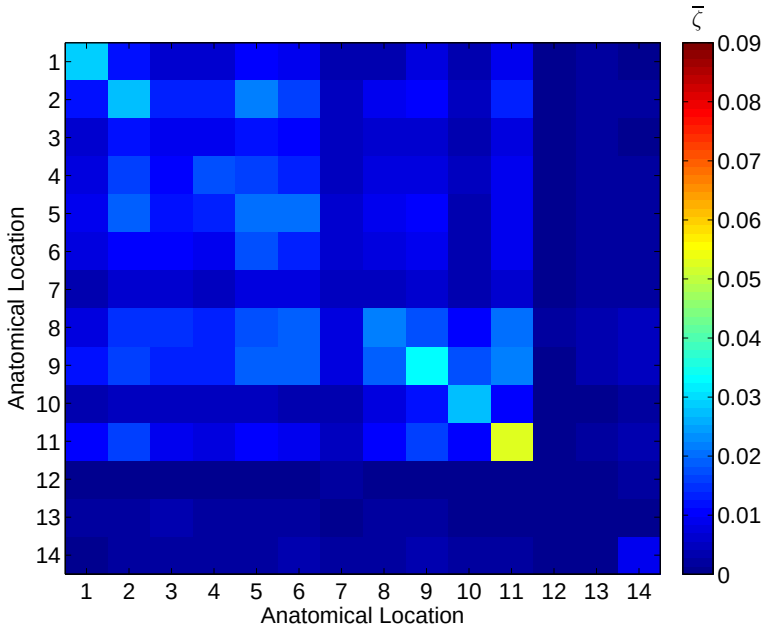

Figure 3.7 : Electrode averaged matrix of regional maximum SdDTF values solved for from ECoG data preprocessed using Preprocessing Method 2 and AMVAR models using orders given by the BIC.

parison. Second, these results describe the maximum SdDTF values reached between regions over the entire task. Stages of speech production models cannot be extracted from these results as the method currently stands. In order to draw deeper conclusions about timings and mechanisms involved in speech production that are specific to the Wordstem task, adjustments will have to be made to the current techniques. For instance, this method can be applied to shorter time blocks that correspond with the timings of the Levelt, Roelofs, and Meyer model of speech production so that the evolution through the duration of the entire task is captured.

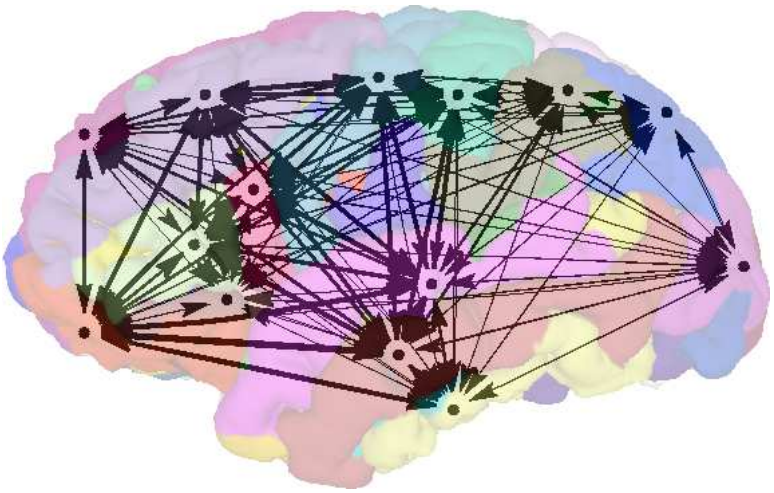

Figure 3.8 : Electrode averaged graph of maximum SdDTF between regions from ECoG data preprocessed using Preprocessing Method 1 and AMVAR models using orders given by the AIC.

An additional direction of this research is exploring nonparametric Granger causality techniques to identify causal influences. Other data measurement modalities, such as cortico-cortical evoked potentials or fMRI, could be incorporated to these results to build more accurate models of ECoG measurements. Studying analytic models of how potentials dissipate in the brain is another route that could be taken with this research.

This work sought to identify cortical areas causally influencing each other during a language task. A new method of analyzing ECoG data was introduced that generates graphical representations of directionality and magnitudes of these influences occurring between brain regions. This method is important because it aggregates

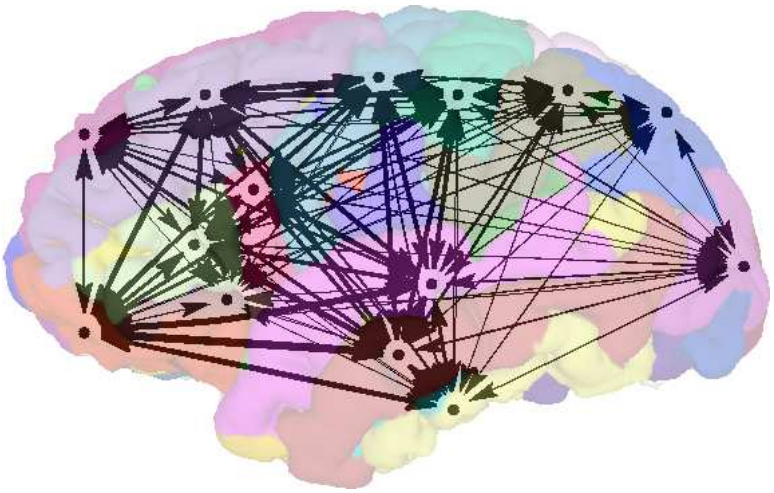

Figure 3.9 : Electrode averaged graph of maximum SdDTF between regions from ECoG data preprocessed using Preprocessing Method 2 and AMVAR models using orders given by the AIC.

significantly larger sets of ECoG data relative to other modern studies, further validating these results. The graphical representations generated by this research can help neurosurgeons identify brain regions crucial for language, taking more care to avoid them, if possible, during medical procedures.

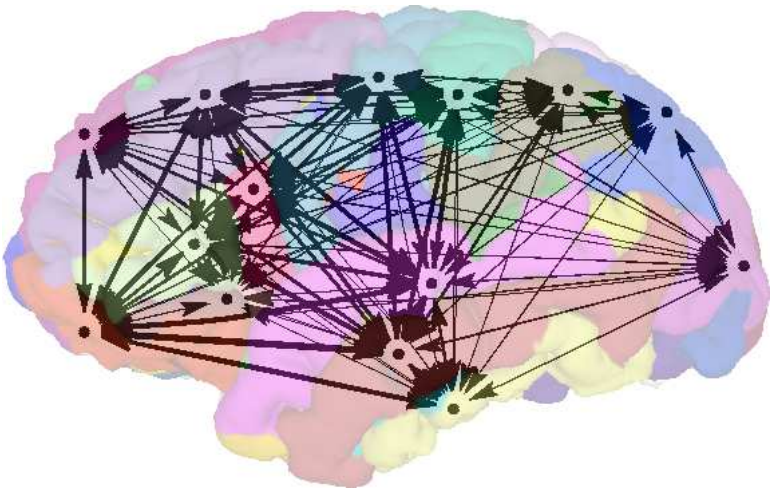

Figure 3.10 : Electrode averaged graph of maximum SdDTF between regions from ECoG data preprocessed using Preprocessing Method 1 and AMVAR models using orders given by the BIC.

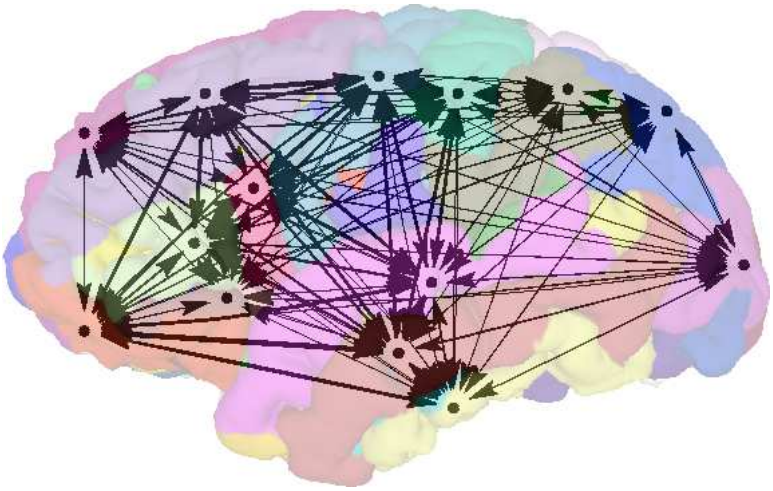

Figure 3.11 : Electrode averaged graph of maximum SdDTF between regions region from ECoG data preprocessed using Preprocessing Method 2 and AMVAR models using orders given by the BIC.

Bibliography

[1] Matthew J. Brookes, Joanne R. Hale, Johanna M. Zumer, Claire M. Stevenson, Susan T. Francis, Gareth R. Barnes, Julia P. Owen, Peter G. Morris, and Srikantan S. Nagarajan. Measuring functional connectivity using MEG: Methodology and comparison with fcMRI. *NeuroImage*, 56:1082–1104, 2011.

[2] David Cohen. Magnetoencephalography: Detection of the brain's electrical activity with a superconducting magnetometer. *Science*, 175(4022):664–666, February 1972.

[3] Christopher R. Conner, Timothy M. Ellmore, Thomas A. Pieters, Michael A. DiSano, and Nitin Tandon. Variability of the relationship between electrophysiology and BOLD-fMRI across cortical regions in humans. *The Journal of Neuroscience*, 36:12855–12865, 2011.

[4] Steven J. Cox and Fabrizio Gabbiani. *Mathematics for Neuroscientists*. Elsevier, first edition, 2010.

[5] Mingzhou Ding, Steven L. Bressler, Weiming Yang, and Hualou Liang. Short-window spectral analysis of cortical event-related potentials by adaptive multivariate autoregressive modeling: data preprocessing, model validation, and variability assessment. *Biological Cybernetics*, 83:35–45, 2000.

[6] Mingzhou Ding, Yonghong Chen, and Steven L. Bressler. Granger causality: Basic theory and application to neuroscience. In B. Schelter, M. Winterhalder, and J. Timmer, editors, *Handbook of Time Series Analysis: Recent Theoretical Developments and Applications*, pages 437–460. WILEY-VCH, 2006.

[7] Erik Edwards, Srikantan S. Nagarajan, Sarang S. Dalal, Ryan T. Canolty, Heidi E. Kirsch, Nicholas M. Barbaro, and Robert T. Knight. Spatiotemporal imaging of cortical activation during verb generation and picture naming. *NeuroImage*, 50:291–301, March 2010.

[8] P. Indefrey and W.J.M. Levelt. The spatial and temporal signatures of word production components. *Cognition*, 92:101–144, 2004.

[9] Maciej Kamiński, Mingzhou Ding, Wilson A. Truccolo, and Steven L. Bressler. Evaluating causal relations in neural systems: Granger causality, directed

transfer function and statistical assessment of significance. *Biological Cybernetics*, 85:145–157, 2001.

[10] Anna Korzeniewska, Ciprian M. Crainiceanu, Rafal Kuś, Piotr J. Franaszczuk, and Nathan E. Crone. Dynamics of event-related causality in brain electrical activity. *Human Brain Mapping*, 29:1170–1192, 2008.

[11] Anna Korzeniewska, Ciprian M. Crainiceanu, Rafal Kuś, Piotr J. Franaszczuk, and Nathan E. Crone. Dynamics of large-scale cortical interactions at high gamma frequencies during word production: Event related causality (ERC) analysis of human electrocorticography (ecog). *NeuroImage*, 56:2218–2237, 2011.

[12] Willem J. M. Levelt, Ardi Roelofs, and Antje S. Meyer. A theory of lexical access in speech production. *Behavioral and Brain Sciences*, 22:1–75, 1999.

[13] Willem J.M. Levelt, Peter Praamstra, Antje S. Meyer, Päivi Helenius, and Riitta Salmelin. An MEG study of picture naming. *Journal of Cognitive Neuroscience*, 10:553–567, 1998.

[14] Tim Mullen. *Source Information Flow Toolbox (SIFT): An Electrophysiological Information Flow Toolbox for EEGLAB Theoretical Handbook and User Manual*. Swartz Center for Computational Neuroscience and Institute for Neural Computation and Department of Cognitive Science, University of California, San Diego, December 2010.

[15] Paul L. Nunez and Ron D. Katznelson. *Electric Fields of the Brain: The Neurophysics of EEG*. Oxford University Press, 1981.

[16] Anthony Ritaccio, Data Boatman-Reich, Peter Brunner, Mackenzie C. Cervanka, Andrew J. Colr, Nathan Crone, Robert Duckrow, Anna Korzeniewska, Brian Litt, Kai J. Miller, Daniel W. Moran, Josef Parvizi, Jonathan Viventi, Justin Williams, and Gerwin Schalk. Proceedings of the second international workshop on advances in electrocorticography. *Epilepsy & Behavior*, 22:641–650, December 2011.

[17] Jr. S. Lawrence Marple. *Digital Spectral Analysis with Applications*. Prentice-Hall, Inc., Englewood Cliffs, New Jersey 07632, 1987.

[18] Ned T. Sahin, Steven Pinker, Sydney S. Cash, Donald Schomer, and Eric Halgren. Sequential processing of lexical, grammatical, and phonological information within Broca's area. *Science*, 326(5951):445–449, October 2009.

[19] Anil K. Seth. *Granger Causal Connectivity Analysis: A MATLAB Toolbox*. University of Sussex, January 2011.

[20] Wolf Singer. Synchronization of cortical activity and its putative role in information processing and learning. *Annual Review of Physiology*, 55:349–374, 1993.

[21] Nitin Tandon. Tandon research lab. http://web.mac.com/ntandon/iWeb/Site/Personnel.html. Accessed March 21, 2012.